Economic Geology, v. 115, no. 4, pp. 871–901

Linking Mineralogy to Lithogeochemistry in the Highland Valley Copper District: Implications for Porphyry Copper Footprints

Kevin Byrne,[1,†] Guillaume Lesage,[2] Sarah A. Gleeson,[3,4] Stephen J. Piercey,[5] Philip Lypaczewski,[1] and Kurt Kyser[6,*]

[1]*Department of Earth and Atmospheric Sciences, University of Alberta, 1-26 Earth Sciences Building, Edmonton, Alberta T6G 2E3, Canada*

[2]*Mineral Deposit Research Unit, The University of British Columbia, #2020–2207 Main Mall, Vancouver, British Columbia V6T 1Z4, Canada*

[3]*Helmholtz Centre Potsdam, GFZ German Research Centre for Geosciences, Telegrafenberg, Potsdam 14772, Germany*

[4]*Institute of Geological Sciences, Freie Universität Berlin, Malteserstrasse 74-100, Berlin 12249, Germany*

[5]*Department of Earth Sciences, Memorial University of Newfoundland, St. John's, Newfoundland A1B 3X5, Canada*

[6]*Department of Geological Sciences and Geological Engineering, Queen's University, Kingston, Ontario K7L 3N6, Canada*

Abstract

The Highland Valley Copper porphyry deposits, hosted in the Late Triassic Guichon Creek batholith in the Canadian Cordillera, are unusual in that some of them formed at depths of at least 4 to 5 km in cogenetic host rocks. Enrichments in ore and pathfinder elements are generally limited to a few hundred meters beyond the pit areas, and the peripheral alteration is restricted to narrow (1–3 cm) halos around a low density of prehnite and/or epidote veinlets. It is, therefore, challenging to recognize the alteration footprint peripheral to the porphyry Cu systems. Here, we document a workflow to maximize the use of lithogeochemical data in measuring changes in mineralogy and material transfer related to porphyry formation by linking whole-rock analyses to observed alteration mineralogy at the hand specimen and deposit scale.

Alteration facies and domains were determined from mapping, feldspar staining, and shortwave infrared imaging and include (1) K-feldspar halos (potassic alteration), (2) epidote veins with K-feldspar–destructive albite halos (sodic-calcic alteration), (3) quartz and coarse-grained muscovite veins and halos and fine-grained white-mica–chlorite veins and halos (white-mica–chlorite alteration), and two subfacies of propylitic alteration comprising (4) prehnite veinlets with white-mica–chlorite-prehnite halos, and (5) veins of epidote ± prehnite with halos of chlorite and patchy K-feldspar. Well-developed, feldspar-destructive, white-mica alteration is indicated by (2[Ca-C] + N + K)/Al values <0.85, depletion in CaO and Na_2O, enrichment in K_2O, and localized SiO_2 addition and is spatially limited to within ~200 m of porphyry Cu mineralization. Localized K_2O, Fe_2O_3, and depletion in Cu, and some enrichment in Na_2O and CaO, occurs in sodic-calcic domains that form a large (~34 km^2) nonconcentric footprint outboard of well-mineralized and proximal zones enriched in K. Water and magmatic CO_2-rich propylitic and sodic-calcic–altered rocks form the largest lithogeochemical footprint to the mineralization in the Highland Valley Copper district (~60 km^2). Calcite in the footprint is interpreted to have formed via phase separation of CO_2 from a late-stage magmatic volatile phase.

Several observations from this study are transferable to other porphyry systems and have implications for porphyry Cu exploration. Feldspar staining and shortwave infrared imaging highlight weak and cryptic alteration that did not cause sufficient material transfer to be confidently distinguished from protolith lithogeochemical compositions. Prehnite can be a key mineral phase in propylitic alteration related to porphyry genesis, and its presence can be predicted based on host-rock composition. Sodic-calcic alteration depletes the protolith in Fe (and magnetite) and, therefore, will impact petrophysical and geophysical characteristics of the system. Whole-rock loss on ignition and C and S analyses can be used to map enrichment in water and CO_2 in altered rocks, and together these form a large porphyry footprint that extends beyond domains of enrichment in ore and pathfinder elements and of pronounced alkali metasomatism.

Introduction

Calc-alkalic porphyry deposits typically have a predictable spatial and temporal distribution of alteration minerals that is the result of the thermal, mechanical, and chemical evolution of the magmatic-hydrothermal system (Seedorff et al., 2005; Sillitoe, 2010). The alteration zones are diagnostic of the fluid composition and temperatures in which they formed and are commonly depicted as volumes of altered rocks in and around Cu mineralization. The deep and central part of the hydrothermal system is characterized by potassic alteration that zones upward to sericitic and then advanced argillic alteration (Seedorff et al., 2005; Sillitoe, 2010). Additionally, at deep levels, potassic alteration can zone laterally into sodic-calcic or propylitic alteration (Seedorff et al., 2008; Halley et al., 2015), whereas at intermediate and shallow levels the peripheral alteration comprises propylitic and intermediate argillic assemblages (Seedorff et al., 2005; Sillitoe,

[†]Corresponding author: e-mail, kbyrne@ualberta.ca
[*]Deceased August 29, 2017

ISSN 0361-0128; doi:10.5382/econgeo.4733; 31 p.
Digital appendices are available in the online Supplements section.

2010). Thus, the plan view distribution of the alteration facies (i.e., the porphyry footprint, which is commonly mapped at surface) is partly a function of erosional level. A challenge for explorationists is that the peripheral parts of porphyry Cu systems are most commonly characterized by green rock propylitic alteration that lacks the diagnostic enrichment in pathfinder elements that occurs with sulfide mineralization and/or sericite alteration (Halley et al., 2015). Propylitic alteration manifests as low- to moderate-intensity replacement of primary feldspars and mafic minerals by epidote-calcite-chlorite (± albite, actinolite, pyrite, hematite, prehnite, and zeolites) and is typically associated with veins of epidote ± chlorite ± carbonate (Meyer and Hemley, 1967; Cooke et al., 2014a, b). Propylitic alteration can extend for several kilometers away from the well-mineralized potassically and hydrolytically altered zones (Seedorff et al., 2005; Cooke et al., 2014a) and, thus, forms the largest footprint. Sodic-calcic or sodic alteration has also been recognized in the peripheral and deep (root) parts of several Laramide porphyry systems in the western part of the United States (Dilles and Einaudi, 1992; Seedorff et al., 2008; Runyon et al., 2019) and in some porphyry Cu systems in British Colombia (Jago et al., 2014; Byrne et al., 2020). Sodic-calcic alteration is characterized by the replacement of K-feldspar and/or plagioclase with albite ± fine-grained white mica and the alteration of mafic minerals to actinolite ± epidote, chlorite, and titanite, which generally occurs with veins of epidote or actinolite (Dilles and Einaudi, 1992; Runyon et al., 2019; Byrne et al., 2020).

Few studies have tested for lithogeochemical changes in the altered rocks peripheral to Cu centers and pyrite halos, particularly at the district scale (e.g., Urqueta et al., 2009; Greenlaw, 2014; Ahmed et al., 2019); nevertheless, some commonalities emerge. By many definitions, propylitic alteration involves material transfer of H_2O, CO_2, and localized S to the altered rocks but limited hydrolysis or alkali exchange metasomatism (Meyer and Hemley, 1967; Ulrich and Heinrich, 2001; Urqueta et al., 2009). In contrast to propylitic facies, sodic-calcic and sodic alteration causes exchange of K for Na, with varying degrees of Ca and CO_2 addition, and can be accompanied by formation of hydrous minerals (Carten, 1986; Dilles and Einaudi, 1992). There is a paucity of studies that assess the district-scale spatial variation of the volatile components (H_2O, OH, CO_2) in the porphyry footprint (e.g., Djouka-Fonkwe et al., 2012).

Four major porphyry Cu-(Mo) deposits occur in the Highland Valley Copper district in British Columbia and constitute Canada's largest and longest-operating Cu mine (Fig. 1; Ydon, 2007; Byrne et al., 2013; Sillitoe, 2013). The Highland Valley Copper porphyry systems are hosted in the Late Triassic Guichon Creek batholith and are unusual in that some of them formed at depths of at least 4 to 5 km (D'Angelo, 2016; D'Angelo et al., 2017). Furthermore, ore (Cu, Mo, Ag) and pathfinder element (e.g., As, Bi, W, Te) concentrations drop to background levels just a few hundred meters beyond the porphyry Cu mineralization (and pit margins), and alteration in the plutonic host rock is restricted to generally narrow 1- to 3-cm halos around a low density of prehnite and/or epidote veinlets (Olade and Fletcher, 1975, 1976; Lesage et al., 2016). This is a particularly challenging style of footprint to explore, because outside of the mine pit areas the geophysical response of the porphyry systems is subdued (Ager et al., 1972; Roy and Clowes, 2000; Byrne et al., 2019; Vallée et al., 2019). The question, then, is how to use lithogeochemistry, in conjunction with mapping, to the best effect in such a challenging environment. As part of the Natural Sciences and Engineering Research Council (NSERC)-Canadian Mining Innovation Council Mineral Exploration Footprints Research Network (Lesher et al., 2017) the footprint of the Highland Valley Copper porphyry district has been investigated. We used feldspar staining, short-wave infrared (SWIR) spectral imaging, and optical microscopy to characterize vein and alteration mineralogy in rock slabs and to categorize the corresponding lithogeochemical samples. We applied molar element ratio (MER) diagrams (Stanley and Madeisky, 1994) and calculate element gains and losses (Grant, 1986). This allowed us to quantify mineralogical changes and material transfer and, thus, evaluate alteration processes.

By linking the observed alteration mineralogy to the lithogeochemical data, we tested how sensitive whole-rock determinations are in detecting changes in mineralogy (and material transfer) in the porphyry footprint. We show that the host-rock composition influences the alteration mineralogy, that material transfer occurred in the green rock outboard of mineralization, and that feldspar staining can identify subtle alteration that cannot be determined from lithogeochemistry. Additionally, we examine the paragenetic origin of secondary calcite and how it contributes to the porphyry footprint. Therefore, this contribution outlines methodologies and approaches that will be useful in elucidating the hydrothermal footprint in porphyry Cu systems globally.

Background Geology

Regional geology

The Quesnel terrane in the Canadian Cordillera is characterized by Mesozoic island-arc assemblages, including the Triassic Nicola Group (Coney et al., 1980). The Nicola Group (Fig. 1B) comprises mafic to intermediate volcaniclastic and volcanogenic sedimentary rocks, sandstone, limestone, layered siltstone, calcareous siltstone, and several chert horizons that were predominantly deposited in a submarine setting (McMillan, 1976, 1977; McMillan et al., 2009). The Triassic Guichon Creek batholith, the host of the Highland Valley Copper deposits, is an I-type composite batholith (D'Angelo et al., 2017) that intruded Nicola Group rocks along the western margin of the Quesnel terrane (Logan and Mihalynuk, 2014).

District-scale geologic framework

The Guichon Creek batholith formed from multiple pulses of magmatism, is compositionally and concentrically zoned, with an oval shape measuring approximately 60 × 25 km, and is elongate to the northwest (Fig. 1). The initial magmatic pulse consists of mafic mineral-rich quartz-diorite, monzogabbro, and granodiorites (the Border, Guichon, and Chataway units), which occur at the margin of the batholith. The second pulse comprises mafic, mineral-poor, quartz-rich granodiorites and monzogranite facies (Bethlehem, Skeena, and Bethsaida; Fig. 1B; D'Angelo et al., 2017; Lee et al., 2020). Syn- to late-mineralization stocks and dikes occur at some of the porphyry centers (Byrne et al., 2013, 2020). The Highland Valley Cop-

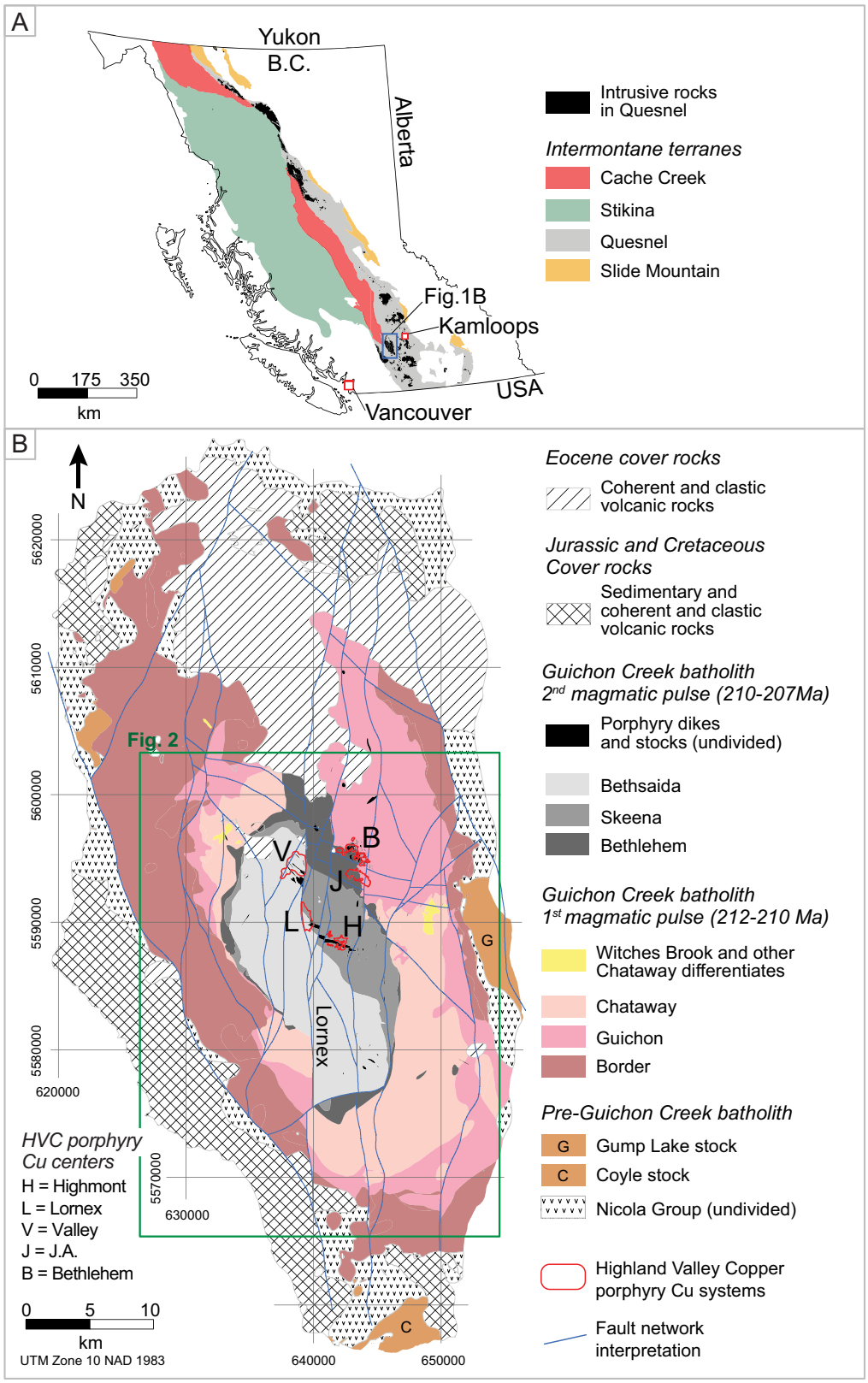

Fig. 1. A. Terranes of the Intermontane belt in British Columbia (B.C.), and the location of the Guichon Creek batholith in the Triassic Quesnel terrane. B. Guichon Creek batholith geology showing the location of the Highland Valley Copper (HVC) porphyry deposits (modified after McMillian et al., 2009; D'Angelo et al., 2017). Note the offset of the Bethsaida granodiorite contact across the Lornex fault and the segmented Valley-Lornex porphyry center. Highmont is spatially associated with an elongate composite dike complex.

per district is situated within the younger, more felsic facies in the core of the batholith and comprises the Bethlehem, J.A., Valley-Lornex, and Highmont porphyry Cu-(Mo) systems (Fig. 2A). Postmineralization faulting along the Lornex fault offset the once contiguous Valley-Lornex system (McMillan, 1974; Hollister et al., 1975).

At least two main stages of porphyry Cu mineralization are evident in the Highland Valley Copper district. The first was at the Bethlehem center at ~209 Ma and is associated with magmatic-hydrothermal breccias and cogenetic porphyry dikes that were emplaced in a dome-shaped feature at the Guichon-Bethlehem granodiorite contact (Briskey and Bellamy, 1976; Briskey, 1980; Byrne et al., 2013; D'Angelo et al., 2017). Bornite and chalcopyrite mineralization is focused in the breccia and synmineralization dikes and occurs with potassic alteration that zones up, and outward, to fine-grained white-mica–chlorite veins and alteration. Mineralization also occurs in D-type veins peripheral to the Cu center (Table 1). Late- to postmineralization stocks, compositionally similar to the Skeena facies, crosscut mineralized breccia at depth in the Bethlehem porphyry center (Byrne et al., 2013). Sodic-calcic alteration overprints potassic facies and Cu mineralization at Bethlehem and is spatially associated with postmineral Skeena stocks emplaced beneath the porphyry center (Byrne et al., 2020). The timing of alteration and mineralization at J.A. is undefined; however, the mineralization and alteration style suggests it is akin to Bethlehem (McMillan, 1985b). Mineralization at Bethlehem was followed by the intrusion and crystallization of the Skeena and Bethsaida facies and, subsequently, the formation of the Valley-Lornex and Highmont porphyry centers between 208 and 207 Ma (D'Angelo et al., 2017). The Valley-Lornex porphyry is hosted in Skeena and Bethsaida granodiorite. Weak chalcopyrite mineralization occurs with early-stage quartz veinlets with narrow K-feldspar halos and is centered on a core domain of Cu-barren quartz veins (Table 1). Main-stage Cu mineralization is represented by quartz-bornite-chalcopyrite ± molybdenite veins with halos of coarse-grained, gray-colored, Na-bearing muscovite (Table 1; Alva-Jimenez et al., 2020) and predominately overprints sodic-calcic alteration (Byrne et al., 2020). Chalcopyrite mineralization also occurs in veins with fine-grained white-mica–chlorite halos at Valley-Lornex and Highmont (Byrne et al., 2013) and in structurally controlled D-type veins that are present up to ~1 km away from the porphyry centers (Table 1). Weak late-stage intermediate-argillic alteration occurs throughout the Valley system (Jambor and Delabio, 1978), but more intense clay alteration is found in fault zones.

Methods

Mapping and sample workflow

Outcrop mapping, core logging, and lithogeochemical sampling was conducted between 2013 and 2016. Mapped alteration captures domains of specific assemblages with similar vein densities or alteration intensity (Fig. 2A).

Representative, coherent blocks with samples of fractures, veins (800–1,000 cm^3), and their alteration assemblages were taken at every available outcrop, typically at a spacing of 0.5 to 1.5 km apart (Fig. 2B). The sample blocks were portioned and slabbed using a rock saw to ensure weathered and organic material was removed before analyses. This methodology was intended to standardize the samples. A total of 867 samples underwent lithogeochemical analysis, feldspar staining, and SWIR spectral imaging. Lithogeochemical data for an additional 181 samples were provided by Teck Resources Limited and are utilized in the maps in this contribution.

Observations made from rock slabs, feldspar staining, and SWIR spectral imaging were integrated to define the alteration facies present in each sample (Table 1). Results were tabulated and linked to the corresponding lithogeochemical analysis (App. 1).

Lithogeochemical analysis

The lithogeochemical analyses were carried out at the Bureau Veritas Laboratories, Vancouver, Canada. A crushed sample split was fused with a lithium metaborate/tetraborate mix. The fused bead was digested using a four-acid solution, and the major element oxides were analyzed by inductively coupled plasma-emission spectroscopy (ICP-ES). Trace elements were measured on an inductively coupled plasma-mass spectrometer (ICP-MS). Loss on ignition (LOI) is reported as percent weight loss on a 1 g sample ignited at 1,000°C. Carbon and S were measured by LECO. Sample preparation, analytical digestion methods, and quality assurance and control procedures are provided in Appendix 2. Total C (wt %) was converted to CO_2, and then the amount of CO_2 and S in each analysis was subtracted from the LOI measurement to estimate the total mineral-hosted H_2O and OH in the sample; this is referred to as the calculated H_2O-OH. The calculated H_2O-OH term assumes all the S in the rock occurs in sulfide minerals—a reasonable assumption for the district samples (see App. 3).

SWIR spectral imaging and feldspar staining

Rock slabs were analyzed using a Specim SisuROCK imaging spectrometer at the University of Alberta, which acquires reflectance data in the SWIR wavelength (λ) range of 1,000 to 2,500 nm, at a variable spatial resolution of 0.2 to 1 mm/pixel (App. 2). Absorption positions were retrieved from the second derivative of interpolated spectra, as described in Lypaczewski and Rivard (2018). The term "white mica" as used herein encompasses the end-member minerals and compositional varieties between muscovite, aluminoceladonite, phengite, and illite. In this study, the λ absorption position of the white-mica Al-OH feature is classified as short (2,190–2,198 nm), intermediate (2,198–2,204 nm), and long (2,204–2,214 nm); see Appendix 2 for more details. This classification is based on the response of the white mica in fracture halos or the background response if no discrete vein halo is present. Prehnite was identified from the SWIR spectra based on a distinct absorption feature appearing at 1,476 nm, and kaolinite is identified by the presence of an absorption around 2,160 nm.

Rock slabs were etched with hydrofluoric acid and stained with sodium cobaltinitrite to detect K-feldspar and with amaranth to test for plagioclase, calcite, and prehnite. Additional information on the interpretation of staining results is provided in Appendix 2.

Whole-rock carbonate C isotope analysis

The $\delta^{18}O$ and $\delta^{13}C$ values of carbonate in 30 whole-rock pulps were determined by reacting approximately 10 to 100 mg of

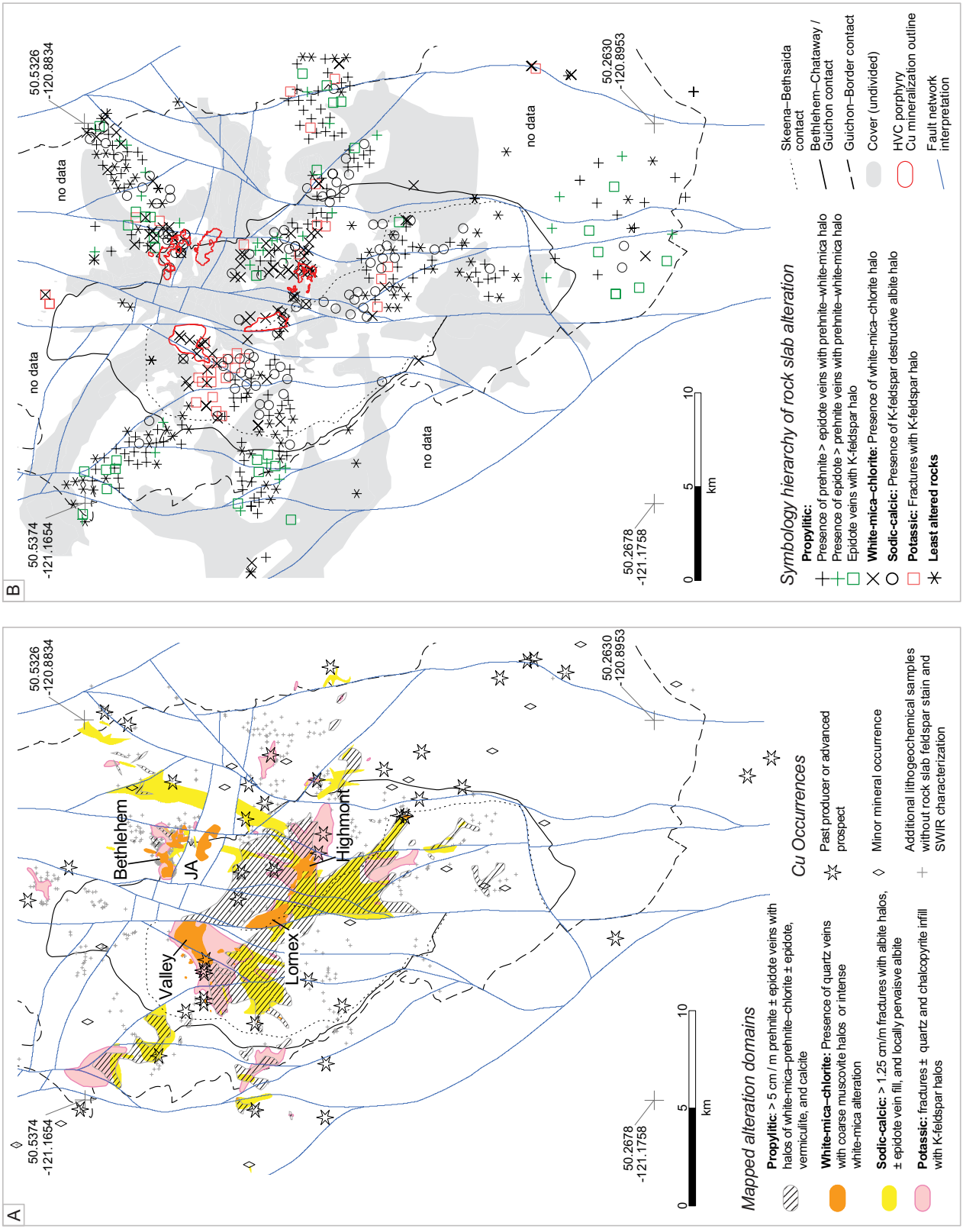

Fig. 2. A. Mapped alteration in the Guichon Creek batholith (modified from McMillian et al., 2009; Lesage et al., 2016) and the location of select Cu occurrences in the region (data from http://aris.empr.gov.bc.ca; http://minfile.gov.bc.ca). Interpretive fault network after Lesage et al., 2019. Additionally, the locations of supplemental lithogeochemical samples, provided by Teck Resources Limited, are indicted. B. Sample (Canadian Mining Innovation Council data) location map showing simplified alteration facies based on feldspar staining, SWIR spectral response, and visual inspection. Some overlapping samples have been removed for clarity. HVC = Highland Valley Copper.

Table 1. Summary of Vein and Alteration Facies in the Highland Valley Copper District and Guichon Creek Batholith

Alteration facies: Vein-(halo)[1]	Fracture fill minerals	Alteration halo minerals	Genetic name	Description	White-mica SWIR Al-OH response[2]	Paragenesis	Location in system	Inferred temperature range (°C)[3]
Barren quartz[4]	Qz,	Weak Ksp, qz	A veins	Sugary texture qz veins (1–3 cm) with localized poorly developed Ksp halos; locally associated with vein dikes and unidirectional solidification textures at depth in Valle	NA	Cut by synmineral qz–(musc) veins	Absent in Bethlehem and Highmont; deep and centrally located in Valley and Lornex	400–500 (Seedorff et al., 2005)
(K-feldspar)	Qz, cp, tour	Ksp, bt, {cp}	Potassic (B veins)	Fracture halos (0.2–1 cm) of Ksp (after plag) associated with discontinuous qz and cp fill; hbl altered to secondary bt	NA	Possibly coeval with the barren qz vein facies and are crosscut by well-mineralized qz-(musc) facies	Bt and Ksp within Cu zones at Bethlehem, Valley, Lornex, and Highmont; extends outboard of Valley and Highmont for several km as weakly mineralized narrow Ksp fracture halos	350–550 (Seedorff et al., 2005)
Epidote-(albite)	Ep, act, diop, tour	Ab, chl, ep, act, wm, gt {tit}	Sodic-calcic, sodic	Ep veins (0.1–1.5 cm) with irregular and diffuse vein walls and Ksp-destructive halos of ab, ab-wm or ab-ep; mafics strongly altered to chl ± act within halo; mt typically altered to Ti oxides; plag is also ab altered in intense alteration; turbidity in altered feldspars caused by microporosity and mineral inclusions; commonly overprinted by prh-wm halos, and rare samples have zoned halos with outer prh-wm halos	Short-λ	Postmineral timing at Bethlehem, mostly premineral at Valley and Lornex, and pre- and post-mainmineral at Highmont where observed together	Pervasive ab and act ± diop are more common proximal to the HVC porphyry centers; structurally controlled, ~0.5–1.5-km-wide, NNE-elongated domain that that is up to ~8 km long in the northeast portion of the batholith, whereas it forms a ~3-km-wide domain that extends for ~7 km south of Lornex and Highmont	300–450 (Seedorff et al., 2005)
(White mica-chlorite)[5]								
Quartz-(muscovite)	Qz, bn, cp, anh	Coarse-grained gray-colored musc, bn, Ksp, qz {hm, rt}	White mica-chlorite[5]	Vitreous qz veins with distinctive coarse-grained 0.3–1.5-cm pale-gray-colored musc (phengitic; Alva-Jimenez et al., 2020) ± intergrown fine-grained Ksp that exhibits bowtie and sericite-island textures (Alva-Jimenez, 2011; Riedell and Proffett, 2014); primary Ksp and bt generally stable and plagioclase is replaced; interpreted to be early-halo-type veins (Proffett, 2009; Alva-Jimenez et al., 2020)	Dominantly short-λ; localized intermediate-λ	Crosscuts ep-(ab) veins and is overprinted by younger faulted hosted qz-ca-mo-py-(wm-chl) veins	Intimately associated with bn and cp mineralization at Valley, Lornex, and locally at Highmont centers; coarse-grained gray and colored musc occurs at some Cu occurrences in the district (Alva-Jimenez et al., 2020)	350–450 (Seedorff et al., 2005)
(White mica-chlorite)	Qz, cp, tour, py, mo, ca, wm	Fine-grained white- to green-colored wm, chl, cp, py, ca, {hm, tit, rt}	White mica-chlorite[5]	Fracture and veinlet (qz and cp) controlled, and locally pervasive, fine-grained white to pale minty-green-colored wm in feldspar sites and chl in mafic sites (i.e., sericitic; Seedorff et al., 2005); locally intense and texturally destructive halos (0.1–1 m) associated with faults containing specularite, qz, cc, and py ± cp fill (i.e., D veins; Seedorff et al., 2005)	Intermediate and long-λ	Mostly crosscuts ep-(ab) and overprints qz-(musc) domains	Intimately associated with qz veins and Cu mineralization at Bethlehem, J.A., and Highmont; fault-controlled D veins extend up to 1 km N and NE of Bethlehem, and 1 km NE of Highmont; occurs peripheral to and crosscuts early halo vein domains at Valley and Lornex; common at Cu occurrences throughout the district	250–350 (Seedorff et al., 2005)

Table 1. (*Cont.*)

Alteration facies: Vein-(halo)[1]	Fracture fill minerals	Alteration halo minerals	Genetic name	Description	White-mica SWIR Al-OH response[2]	Paragenesis	Location in system	Inferred temperature range (°C)[3]
(Intermediate argillic/clay)[4]		Fine-grained wm, kaol, mont, chl,	Intermediate argillic	Primary bt replaced to brown-colored mixture of wm-mont; plag altered to mixtures of wm-kaol-mont (Jambor and Delabio, 1978); selective replacement of relict plag in previously altered rocks	Kaol interference common	Appears to be late to postmineral; most intense in the barren qz vein core and locally within qtz-(musc) domains at Valley	Generally limited to the Cu mineralized portions of the J.A. and Valley, and parts of Lornex and Highmont; occurs in and around structures hosting late ca, qz, py, mo-(wm-chl) veins	100–200 (Seedorff et al., 2005)
Epidote-(K-feldspar)	Ep, prh, pump, ca, qz	Weak to moderate Ksp, wm, ep, chl, prh, verm, ab	Propylitic	Weak to moderately developed Ksp ± ep halos (0.5–1 cm) associated with ep ± prh veins; irregular and diffuse vein walls; white micas dominantly have a short-λ Al-OH absorption feature; primary Ksp stable; some zoned halos of inner Ksp and outer wm; mafics altered to chlorite	Short-λ	Pre- to syn-prh-(wm-prh) facies	Mostly occurs in the more mafic Guichon and Border granodiorites	200–350 (Digel and Gordon, 1995; Bird and Spieler, 2004; Seedorff et al., 2005)
Prehnite-(white mica-prehnite)	Prh, ep, pump, ca, qz	Prh, wm, ab, chl, ep, pump, verm, ca {cp, mt, hm, tit}	Propylitic	Veinlets (0.1–0.2 cm) of prh ± intergrown ep and ca, ± late pump, with plag-destructive halos of wm-prh and accessory ab; Ksp stable; planar, sharp margins; turbid feldspar in halos; hbl incompletely replaced by chl ± act, ep within halo; primary bt locally altered to chl or verm with prh along cleavage planes; generally sharp vein walls; mt altered to ilm ± hm; localized reddening in the halo	Dominantly short-λ; localized intermediate-λ proximal to the Cu centers	Refractures existing veins and crosscuts earlier formed veins and alteration where observed together	Highest density of veins centered on the HCV porphyry systems but occurs throughout the batholith at lower vein density	200–250 (Digel and Gordon, 1995; Bird and Spieler, 2004; Seedorff et al., 2005)

{} = accessory minerals

Mineral abbreviations: ab = albite, act = actinolite, anh = anhydrite, bn = bornite, bt = biotite, ca = carbonates, chl = chlorite, cp =chalcopyrite, diop = diopside, ep = epidote, gt = garnet, hm = hematite, ill = illite, kaol = kaolinite, Ksp = K-feldspar, mont = montmorillonite, mt = magnetite, musc = muscovite (coarse grained), plag = plagioclase, prh = prehnite, pump = pumpellyite, py = pyrite, qz = quartz, rt = rutile, tit = titanite, tour = tourmaline, verm = vermiculite, wm = white mica undifferentiated between illite, fine-grained muscovite, paragonite, phengite, and montmorillonite; white mica is synonymous with sericite

[1]Parentheses indicate minerals in the halo

[2]The wavelength (λ) position of the Al-OH absorption feature is classified as short (2,190–2,199 nm), intermediate (2,199–2,204 nm), and long (2,204–2,214 nm); prehnite is identified from the SWIR image based on a distinct absorption feature between 1,470 and 1,480 nm

[3]Temperature range estimates based on mineral stabilities presented in the references indicated

[4]Not assessed in this study

[5]Quartz-(muscovite) and (white-mica–chlorite) subfacies are grouped together as "white mica-chlorite" alteration facies in this study

powdered material with 100% anhydrous phosphoric acid at 72°C for 4 h. The CO_2 released was analyzed using a Thermo-Finnigan Gas Bench coupled to a Thermo-Finnigan DeltaPlus XP continuous-flow isotope-ratio mass spectrometer (CF-IRMS) at the Queen's Facility for Isotope Research (QFIR). Sample isotope values are reported using the delta (δ) notation in permil (‰), relative to Vienna Pee Dee Belemnite (VPDB) and Vienna standard mean ocean water (VSMOW), respectively, with precisions of 0.2‰.

MER diagrams

MERs are used to reduce the effects of closure and cast lithogeochemical data in terms that can be related to variations in mineral formulae and chemical reaction stoichiometries and to test for material transfer (Madeisky and Stanley, 1993; Stanley, 2011). More specifically, Pearce element ratio (PER) diagrams use a denominator element that did not participate in material transfer processes. This creates a simple proportionality with material transfer (Madeisky and Stanley, 1993; Stanley and Madeisky, 1994). As a result, it is critical to test whether the chosen denominator is conserved. Figure 3 plots the immobile elements Al versus Ti and Zr for the least altered and altered Guichon Creek batholith rocks. Samples from an originally homogeneous protolith will form a linear array that passes through the origin if the plotted elements are truly immobile, and disparate protoliths will form additional linear arrays and trend lines (Barrett and McLean, 1999; Bushchette and Piercey, 2016). Based on Figure 3, Al, Ti, and Zr are immobile with respect to alteration (i.e., each linear array has a homogeneous protolith). However, there is a variation between different sample suites in terms of Ti, Zr, and several other incompatible elements due to magmatic differentiation in the Guichon Creek batholith (D'Angelo et al., 2017; Lee et al., 2020). Therefore, we cannot apply PER plots sensu stricto to understand magmatic fractionation (Russell and Stanley, 1990). We will demonstrate, however, that by grouping and plotting the data by rock types (defined from a combination of mapping, mineralogical and textural criteria, and Al-Ti compositions) Ti can be used in the denominator in PER plots to elucidate alteration processes.

Assessment of material transfer (element gains and losses)

To assess and visualize element gains, losses, and immobility in select sample pairs, isocon diagrams were constructed (Grant, 1986, 2005). Element gains and losses for each alteration facies, based on median values in the data populations, were calculated using equation (1) on a weight basis following Grant's approach (Grant, 1986; Warren et al., 2007) and using Al_2O_3 as the immobile element (immobility demonstrated below):

$$\Delta C = (CP\ \text{immobile}/CA\ \text{immobile}) \cdot CA - CP, \quad (1)$$

where CP and CA are the concentrations of the immobile element in the protolith (P) and altered (A) sample, respectively, and ΔC denotes the gain or loss in grams per 100 g of rock for major elements, in parts per million for trace elements, and in parts per billion for Au, Ag, and Hg. Common protoliths for the Guichon Creek batholith rock facies were determined on a sample-by-sample basis using the mineralogical, textural, and Al-Ti composition criteria of McMillan (1985a) and D'Angelo et al. (2017).

Results

Least altered rock (protolith) compositions

The least altered samples (Table 2) were identified using spectral and feldspar staining results and defined by the absence of macroscopic veins, halos, or aplite dikes. These samples have primary plagioclase, K-feldspar, and hornblende with a fresh appearance. The Guichon Creek batholith formed from two magmatic pulses that fractionated from high to low Ti at a relatively constant Al content (Fig. 4A; D'Angelo et al., 2017; Whalen et al., 2017). The decrease in Ti corresponds to a decrease in Mg number (Fig. 4B) and an increase in Si (Fig. 4C). On a plot of 2Ca + Na + K/Ti versus Al/Ti (molar) the mineralogical control on the composition of a sample is indicated by the slope of the line made between the origin and the sample (Madeisky and Stanley, 1993). For feldspar-controlled compositions the slope of the plot is 1, 0.3 if muscovite, and 0 for

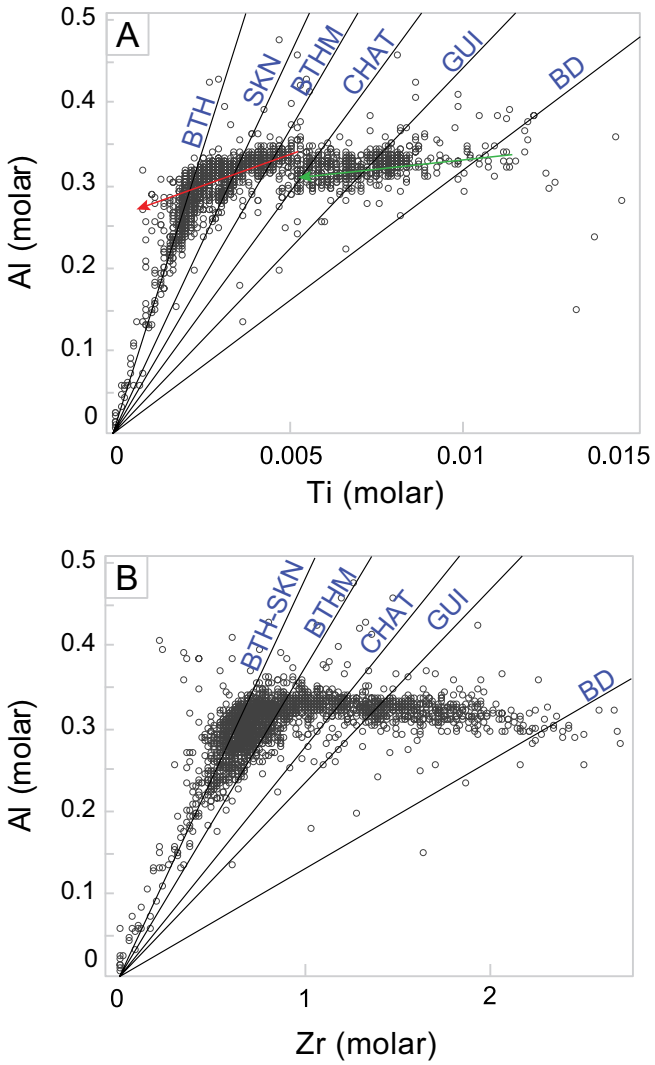

Fig. 3. Immobile and conserved element test cross plots. A. Al versus Ti (molar). B. Al versus Zr (molar). The lines indicating protolith compositions are modified from D'Angelo et al. (2107) and represent the typical least altered composition. The green and red lines represent magmatic evolution trends of the first and second magmatic pulses. Abbreviations: BD = Border, BTH = Bethsaida, BTHM = Bethlehem, CHAT = Chataway, GUI = Guichon, SKN = Skeena.

Table 2. Representative Lithogeochemical Data for the Guichon Creek Batholith

	Border diorite		Guichon and Chataway granodiorite						
	Least altered	σ	Least altered	σ	Epidote-(albite)	K-feldspar	White mica-chlorite[1]	Epidote-(K-feldspar)	Prehnite-(white mica-prehnite)
n	10		39		31	7	14	26	126
SiO_2 (wt %)	58.60	2.11	61.82	1.50	63.42	63.05	60.34	61.10	62.71
Al_2O_3	16.40	0.54	16.42	0.52	15.94	15.81	16.84	16.49	16.30
Fe_2O_3	7.06	0.74	5.39	0.37	3.97	5.14	5.62	5.60	5.02
MgO	3.54	0.50	2.75	0.33	2.22	2.40	2.75	2.83	2.37
CaO	6.30	0.74	5.15	0.50	5.23	3.40	4.32	5.21	4.86
Na_2O	3.56	0.23	4.00	0.20	4.83	3.81	3.93	4.03	4.05
K_2O	1.98	0.39	2.20	0.27	0.68	3.17	2.21	1.94	2.14
TiO_2	0.86	0.12	0.61	0.03	0.57	0.54	0.62	0.61	0.56
P_2O_5	0.18	0.05	0.16	0.01	0.14	0.11	0.16	0.15	0.15
MnO	0.11	0.02	0.08	0.01	0.07	0.06	0.09	0.09	0.08
Cr_2O_3	0.00	0.00	0.00	0.00	0.00	0.00	0.00	0.00	0.00
S	0.01	0.00	0.01	0.00	0.01	0.01	0.01	0.01	0.01
C	0.02	0.01	0.01	0.01	0.10	0.01	0.05	0.02	0.01
LOI	1.3	0.4	1.0	0.3	1.9	1.2	1.6	1.5	1.4
CO_2	0.07	0.03	0.04	0.03	0.37	0.04	0.18	0.07	0.04
Calcite[1]	0.17	0.06	0.08	0.08	0.84	0.08	0.42	0.17	0.08
H_2O-OH[1]	1.2	0.3	1.0	0.3	1.5	1.1	1.4	1.4	1.4
Sc (ppm)	18	2	11	1	10	11	11	12	10
Ba	632	73	699	55	151	841	700	634	694
Cs	1.7	1.2	1.1	0.4	0.9	1.0	0.8	0.8	1.1
Ga	16.9	1.1	17.2	1.0	16.5	16.4	17.5	16.7	17.0
Hf	3.9	11.3	3.7	0.8	3.8	3.3	3.3	3.5	4.1
Nb	3.3	1.1	2.6	0.6	2.8	2.6	2.7	2.5	2.6
Rb	56.9	17.2	57.5	11.7	17.5	91.2	52.6	50.3	54.4
Sn	0.5	0.2	0.5	0.0	0.5	1.0	0.5	0.5	0.5
Sr	544.3	112.4	657.0	67.9	588.8	497.2	645.6	668.3	639.3
Ta	0.3	0.1	0.1	0.1	0.2	0.2	0.2	0.2	0.2
Th	3.6	1.8	4.8	1.6	5.9	5.9	4.8	4.2	4.8
U	2.0	0.8	2.2	0.6	2.5	2.9	2.4	1.9	2.2
V	184	30	138	13	117	117	137	141	128
W	0.6	0.4	0.3	0.3	0.6	0.7	1.3	0.3	0.3
Zr	135.9	480.3	128.9	31.7	135.9	116.4	104.4	119.2	139.6
Y	16.9	3.6	11.6	1.9	13.2	11.4	10.6	11.3	11.9
La	14.3	2.5	14.0	2.0	14.7	15.4	14.1	13.5	14.3
Ce	31.5	6.1	29.5	4.4	31.8	32.7	31.0	30.3	31.0
Pr	4.07	0.77	3.74	0.54	3.86	4.11	3.83	3.71	3.88
Nd	17.1	3.5	15.6	2.2	15.3	16.3	15.9	15.1	16.1
Sm	3.75	0.80	2.98	0.47	3.28	3.15	3.14	3.09	3.18
Eu	0.94	0.15	0.79	0.07	0.76	0.77	0.81	0.83	0.80
Gd	3.61	0.64	2.61	0.44	2.82	2.60	2.49	2.63	2.70
Tb	0.53	0.09	0.38	0.06	0.41	0.40	0.36	0.37	0.40
Dy	3.07	0.49	2.16	0.40	2.51	2.14	2.02	2.11	2.25
Ho	0.56	0.13	0.43	0.07	0.47	0.41	0.41	0.41	0.43
Er	1.77	0.36	1.19	0.21	1.31	1.37	1.13	1.17	1.25
Tm	0.27	0.07	0.19	0.03	0.21	0.19	0.17	0.18	0.19
Yb	1.66	0.36	1.22	0.24	1.30	1.30	1.15	1.21	1.26
Lu	0.28	0.07	0.19	0.03	0.19	0.21	0.18	0.19	0.20
Mo	1.05	0.83	0.58	0.42	0.45	0.63	0.63	0.63	0.59
Cu	148.50	98.31	106.62	49.18	23.19	456.53	359.09	115.92	111.28
Pb	2.00	0.81	1.42	1.56	1.01	1.72	1.23	1.75	1.71
Zn	46.7	3.9	33.2	6.7	33.3	26.0	37.9	37.2	32.6
Ag (ppb)	55	41	40	17	24	208	187	43	42
Ni	15.5	2.4	13.4	2.8	9.2	12.3	15.3	14.6	11.8
Co	14.7	2.3	10.0	1.1	6.5	8.5	10.9	11.3	9.8
Mn	309.0	35.9	252.0	23.8	323.5	238.0	408.5	305.0	283.0
As	2.2	0.6	1.1	0.6	3.9	1.5	1.5	1.2	1.0
Au (ppb)	1.5	0.8	0.9	0.9	0.1	0.1	1.9	1.0	0.8
Cd	0.05	0.03	0.03	0.04	0.01	0.02	0.03	0.03	0.02
Sb	0.11	0.05	0.06	0.04	0.45	0.12	0.16	0.07	0.07
Bi	0.05	0.03	0.04	0.03	0.01	0.06	0.08	0.02	0.03
Cr	20.90	10.76	16.70	5.39	11.75	15.20	16.10	14.75	13.10
B	7	3	3	2	3	6	7	4	4
Tl	0.08	0.03	0.06	0.02	0.02	0.01	0.02	0.02	0.03
Hg (ppb)	9	5	3	2	3	3	4	3	3
Se	0.05	0.02	0.05	0.00	0.05	0.05	0.05	0.05	0.05

Table 2. (*Cont.*)

	Border diorite		Guichon and Chataway granodiorite						
	Least altered	σ	Least altered	σ	Epidote-(albite)	K-feldspar	White mica-chlorite[1]	Epidote-(K-feldspar)	Prehnite-(white mica-prehnite)
n	10		39		31	7	14	26	126
Te	0.01	0.02	0.01	0.00	0.02	0.03	0.03	0.01	0.01
Ge	0.05	0.05	0.05	0.02	0.05	0.05	0.08	0.05	0.05
In	0.01	0.01	0.01	0.00	0.01	0.01	0.01	0.01	0.01
Re (ppb)	0.50	0.00	0.5	0.22	0.5	0.5	0.5	0.5	0.5
Be	0.2	0.1	0.2	0.1	0.3	0.3	0.2	0.3	0.3
Li	8.8	1.2	8.1	1.9	6.9	7.5	7.5	9.0	8.6

	Bethlehem and Skeena granodiorite						
	Least altered	σ	Epidote-(albite)	K-feldspar	White mica-chlorite[1]	Epidote-(K-feldspar)	Prehnite-(white mica-prehnite)
n	17		39	5	23	1	35
SiO_2 (wt %)	66.58	1.24	67.16	68.12	67.00	67.16	67.25
Al_2O_3	16.85	0.45	16.49	16.33	16.38	16.74	16.44
Fe_2O_3	3.30	0.44	2.88	2.88	3.15	3.09	3.08
MgO	1.04	0.18	1.00	0.92	0.97	0.96	0.96
CaO	4.15	0.44	4.31	3.37	3.10	3.82	3.89
Na_2O	4.74	0.16	4.85	4.70	4.57	4.72	4.78
K_2O	1.73	0.24	0.75	2.14	1.87	2.02	1.84
TiO_2	0.33	0.04	0.33	0.29	0.30	0.30	0.30
P_2O_5	0.13	0.01	0.12	0.11	0.12	0.11	0.11
MnO	0.06	0.02	0.04	0.06	0.05	0.07	0.05
Cr_2O_3	0.00	0.00	0.00	0.00	0.00	0.00	0.00
S	0.01	0.00	0.01	0.01	0.02	0.01	0.01
C	0.01	0.02	0.08	0.01	0.09	0.01	0.02
LOI	0.8	0.7	1.9	1.0	1.9	0.8	1.2
CO_2	0.04	0.06	0.29	0.04	0.33	0.04	0.07
Calcite[1]	0.08	0.14	0.67	0.08	0.75	0.08	0.17
H_2O-OH[1]	0.7	0.6	1.6	0.9	1.6	0.8	1.2
Sc (ppm)	4	1	4	4	4	4	4
Ba	815	217	372	954	702	884	850
Cs	0.6	0.6	0.5	1.1	1.0	0.3	0.6
Ga	17.0	2.1	17.0	2.8	15.9	18.9	16.5
Hf	2.2	0.5	2.3	16.0	2.2	2.8	2.2
Nb	1.6	0.6	1.9	2.3	1.5	1.8	1.7
Rb	27.4	8.2	17.5	39.7	29.3	34.4	30.5
Sn	0.5	0.5	0.5	1.8	1.0	2.0	1.0
Sr	712.5	92.1	759.3	647.8	650.5	685.9	662.7
Ta	0.1	0.1	0.1	0.8	0.1	0.1	0.1
Th	1.7	0.7	1.6	0.1	1.4	1.7	1.6
U	0.8	0.5	1.0	1.6	1.0	1.0	1.0
V	62	12	62	57	58	58	58
W	0.3	0.4	0.6	0.7	1.8	0.3	0.3
Zr	72.1	17.5	79.0	1.3	70.5	88.2	72.7
Y	6.1	0.8	6.3	72.6	5.8	5.9	6.0
La	9.3	1.0	9.0	5.7	9.0	9.6	9.5
Ce	18.2	2.2	18.1	0.3	18.0	17.9	18.3
Pr	2.26	0.33	2.22	9.55	2.17	2.11	2.16
Nd	8.9	1.7	9.0	18.6	8.5	8.8	8.7
Sm	1.66	0.32	1.70	2.17	1.60	1.67	1.60
Eu	0.52	0.08	0.52	8.00	0.51	0.54	0.52
Gd	1.40	0.20	1.45	1.51	1.30	1.41	1.35
Tb	0.20	0.03	0.21	0.48	0.19	0.20	0.19
Dy	1.08	0.26	1.12	1.25	1.08	1.13	1.07
Ho	0.21	0.04	0.22	0.19	0.20	0.22	0.21
Er	0.61	0.15	0.64	0.97	0.58	0.60	0.61
Tm	0.09	0.02	0.10	0.20	0.08	0.10	0.09
Yb	0.65	0.13	0.68	0.54	0.64	0.72	0.64
Lu	0.10	0.02	0.11	0.08	0.10	0.12	0.10
Mo	0.07	0.91	0.50	0.48	1.43	0.34	0.28
Cu	17.50	43.12	19.91	193.63	133.06	71.75	14.43
Pb	1.00	0.43	1.86	1.74	1.74	0.73	1.46

Table 2. (*Cont.*)

	Bethlehem and Skeena granodiorite						
	Least altered	σ	Epidote-(albite)	K-feldspar	White mica-chlorite[1]	Epidote-(K-feldspar)	Prehnite-(white mica-prehnite)
n	17		39	5	23	1	35
Zn	23.0	13.6	20.2	24.0	22.4	20.0	21.9
Ag (ppb)	13	16	23	48	56	22	20
Ni	2.5	0.6	2.7	2.3	2.4	2.3	2.3
Co	4.3	1.0	4.3	4.1	4.6	4.1	4.4
Mn	258.5	87.2	204.0	278.0	274.0	314.0	267.0
As	0.7	1.3	1.2	0.1	0.9	0.5	0.7
Au (ppb)	0.2	1.7	0.4	0.5	0.4	0.5	0.2
Cd	0.01	0.07	0.02	0.02	0.02	0.01	0.01
Sb	0.04	0.07	0.15	0.04	0.10	0.11	0.05
Bi	0.01	0.02	0.01	0.03	0.05	0.01	0.01
Cr	4.00	3.46	2.80	1.78	2.90	2.80	3.00
B	2	2	2	1	2	1	2
Tl	0.01	0.02	0.01	0.55	0.02	0.01	0.01
Hg (ppb)	3	3	3	3	5	3	3
Se	0.05	0.02	0.05	0.05	0.05	0.05	0.05
Te	0.01	0.00	0.01	0.02	0.01	0.01	0.01
Ge	0.05	0.00	0.05	0.01	0.05	0.05	0.05
In	0.01	0.00	0.01	0.05	0.01	0.01	0.01
Re (ppb)	0.5	0.00	0.5	0.0	0.5	0.5	0.5
Be	0.1	0.2	0.2	0.5	0.3	0.2	0.3
Li	5.7	6.4	5.6	8.8	5.5	3.1	5.3

	Bethsaida granodiorite							
						Prehnite-(white mica-prehnite)		
	Least altered	σ	Epidote-(albite)	K-feldspar	White mica-chlorite[1]	All samples	Distal	Proximal
n	45		65	30	50	71		
SiO_2 (wt %)	69.33	0.62	69.21	70.25	70.35	69.17	69.02	69.24
Al_2O_3	16.16	0.22	15.93	15.86	14.44	16.03	16.06	16.03
Fe_2O_3	2.32	0.17	2.25	2.14	2.03	2.30	2.40	2.27
MgO	0.60	0.07	0.62	0.55	0.42	0.61	0.69	0.58
CaO	3.05	0.24	3.09	2.67	1.70	2.92	3.05	2.95
Na_2O	4.96	0.17	5.11	4.95	1.65	4.96	4.80	5.00
K_2O	1.89	0.19	1.25	2.09	2.55	1.85	1.92	1.82
TiO_2	0.23	0.01	0.22	0.22	0.17	0.23	0.24	0.22
P_2O_5	0.08	0.01	0.08	0.07	0.07	0.08	0.09	0.08
MnO	0.06	0.01	0.06	0.04	0.04	0.06	0.07	0.05
Cr_2O_3	0.00	0.00	0.00	0.00	0.00	0.00	0.00	0.00
S	0.01	0.00	0.01	0.01	0.19	0.01	0.01	0.01
C	0.01	0.01	0.07	0.01	0.35	0.01	0.01	0.03
LOI	0.9	0.4	1.8	0.9	3.4	1.3	1.4	1.4
CO_2	0.04	0.02	0.26	0.04	1.28	0.04	0.04	0.09
Calcite[1]	0.08	0.06	0.58	0.08	2.92	0.08	0.08	0.21
H_2O-OH[1]	0.8	0.4	1.6	0.9	2.0	1.3	1.4	1.3
Sc (ppm)	3	0	2	2	2	2	3	2
Ba	977	134	732	1,040	744	939	881	949
Cs	0.7	0.3	0.5	0.6	1.5	0.6	0.6	0.6
Ga	16.3	1.0	16.0	16.4	14.9	16.2	15.8	16.4
Hf	2.0	0.2	2.0	2.0	1.8	2.0	2.1	2.0
Nb	1.8	1.3	1.8	2.0	1.7	1.8	1.7	1.9
Rb	30.5	4.0	21.3	32.7	46.2	30.9	31.2	30.7
Sn	0.5	0.1	0.5	0.5	0.5	0.5	0.5	0.5
Sr	635.0	45.6	672.0	615.1	237.7	631.8	629.1	633.2
Ta	0.1	0.1	0.1	0.2	0.1	0.1	0.1	0.1
Th	1.2	0.3	1.1	1.1	0.8	1.3	1.4	1.3
U	0.6	0.2	0.7	0.6	0.6	0.7	0.9	0.7
V	39	5	36	33	31	40	42	38
W	0.3	0.3	0.6	0.6	3.3	0.3	0.3	0.4
Zr	65.4	6.8	66.0	67.0	58.7	66.3	65.8	66.4
Y	5.3	0.9	5.3	5.5	5.0	5.3	5.4	5.3
La	9.4	0.9	9.1	9.9	7.7	9.6	9.9	9.5
Ce	17.4	2.0	17.5	17.7	15.5	17.9	18.9	17.3

Table 2. (*Cont.*)

	Bethsaida granodiorite							
						Prehnite-(white mica-prehnite)		
	Least altered	σ	Epidote-(albite)	K-feldspar	White mica-chlorite[1]	All samples	Distal	Proximal
n	45		65	30	50	71		
Pr	2.03	0.27	2.02	2.04	1.82	2.04	2.11	1.98
Nd	7.8	1.3	7.8	7.9	6.8	8.0	8.5	7.7
Sm	1.33	0.27	1.34	1.35	1.21	1.38	1.42	1.31
Eu	0.44	0.05	0.42	0.41	0.32	0.43	0.45	0.43
Gd	1.13	0.18	1.12	1.15	1.00	1.15	1.21	1.13
Tb	0.16	0.03	0.16	0.16	0.14	0.16	0.16	0.16
Dy	0.93	0.17	0.89	0.88	0.83	0.93	0.96	0.89
Ho	0.18	0.04	0.18	0.18	0.17	0.18	0.18	0.18
Er	0.51	0.10	0.53	0.55	0.51	0.53	0.55	0.52
Tm	0.08	0.02	0.08	0.08	0.08	0.08	0.09	0.08
Yb	0.60	0.09	0.61	0.62	0.58	0.61	0.63	0.60
Lu	0.10	0.01	0.10	0.10	0.10	0.10	0.10	0.10
Mo	0.17	0.33	0.22	1.85	7.11	0.26	0.18	0.33
Cu	6.24	45.41	4.54	370.47	1,632.74	8.68	5.65	15.28
Pb	0.95	0.51	1.70	1.00	1.76	1.63	2.03	1.44
Zn	25.0	6.1	27.6	16.6	14.6	24.4	31.3	22.4
Ag (ppb)	12	39	17	114	614	21	19	21
Ni	1.1	0.3	1.0	1.0	0.6	1.2	1.5	1.1
Co	2.9	0.5	2.8	2.6	1.2	2.8	3.5	2.7
Mn	339.0	52.7	343.0	276.5	302.5	341.0	367.5	327.5
As	0.3	0.4	0.7	0.3	1.7	0.5	0.6	0.4
Au (ppb)	0.4	0.9	0.1	3.0	2.8	0.3	0.1	0.5
Cd	0.01	0.01	0.01	0.01	0.04	0.01	0.01	0.01
Sb	0.02	0.03	0.09	0.03	0.05	0.03	0.04	0.03
Bi	0.01	0.05	0.01	0.07	0.20	0.01	0.01	0.03
Cr	2.40	2.02	2.40	2.10	4.05	2.30	2.75	2.10
B	1	1	1	1	2	2	2	2
Tl	0.01	0.01	0.01	0.02	0.03	0.01	0.01	0.01
Hg (ppb)	3	2	3	4	6	3	3	3
Se	0.05	0.00	0.05	0.05	0.05	0.05	0.05	0.05
Te	0.01	0.01	0.01	0.01	0.03	0.01	0.01	0.01
Ge	0.05	0.04	0.05	0.05	0.05	0.05	0.05	0.05
In	0.01	0.00	0.01	0.01	0.01	0.01	0.01	0.01
Re (ppb)	0.5	0.15	0.5	0.5	2.0	0.5	0.5	0.5
Be	0.2	0.1	0.3	0.2	0.2	0.3	0.4	0.3
Li	6.1	2.7	4.7	4.9	0.9	6.5	8.7	5.5

The median oxide and elemental values for the least altered (protolith) and alteration facies populations are presented; data shown correspond to analysis used in elemental gain and loss calculations and diagrams

[1]Calculated fields based on S, C, and LOI analysis and on the assumption that all CO_2 is associated with $CaCO_3$, and S as sulfide species

chlorite and kaolinite (Stanley and Madeisky, 1994). By plotting the (2Ca + Na + K)/Ti versus Al/Ti slope value against the Al/Ti value, the initial Ca, Na, and K content can be evaluated with respect to magmatic evolution (Fig. 4D). Guichon Creek batholith rocks evolved from high (2Ca + Na + K)/Al values toward compositions controlled by feldspar (Fig. 4D). Least altered Border, Guichon, and Chataway rocks have (2Ca + Na + K)/Al values >1 because of high Ca concentrations (Table 2) associated with hornblende content in excess of 5% (McMillan, 1985a). Unaltered Bethlehem granodiorite has (2Ca + Na + K)/Al between ~1.1 and 1, whereas the Skeena and Bethsaida granodiorites cluster between 1 and 0.95 (Fig. 4D). There is no evidence of primary carbonate (Table 2; D'Angelo, 2016).

Vein and alteration facies characteristics and mapped distribution

Lithogeochemical samples in the Guichon Creek batholith were cataloged into district-scale alteration facies that captured common vein and halo mineralogy based on the feldspar staining and the spectral response from rock slabs (Table 1; Fig 5). The alteration facies outlined below provide the framework for assessing and plotting the lithogeochemical data in subsequent sections.

Potassic: K-feldspar: This facies comprises veinlets and discontinuous fracture fills of quartz and chalcopyrite with 1- to 2-cm K-feldspar halos (Fig. 5A). The highest density (~5 cm/m) of veinlets with K-feldspar halos is located over the Valley deposit. The presence of K-feldspar halos continues, at a lower density, for ~2 km west of known mineralization; beyond this distance they are absent (Figs. 2, 5A). A second K-feldspar halo domain occurs over Lornex and Highmont that extends asymmetrically up to 1 km to the northeast in narrow structures and ~2 km to the southeast (Fig. 2A).

Sodic-calcic: Epidote-(albite): Epidote veins with K-feldspar–destructive albite halos compose the sodic-calcic facies

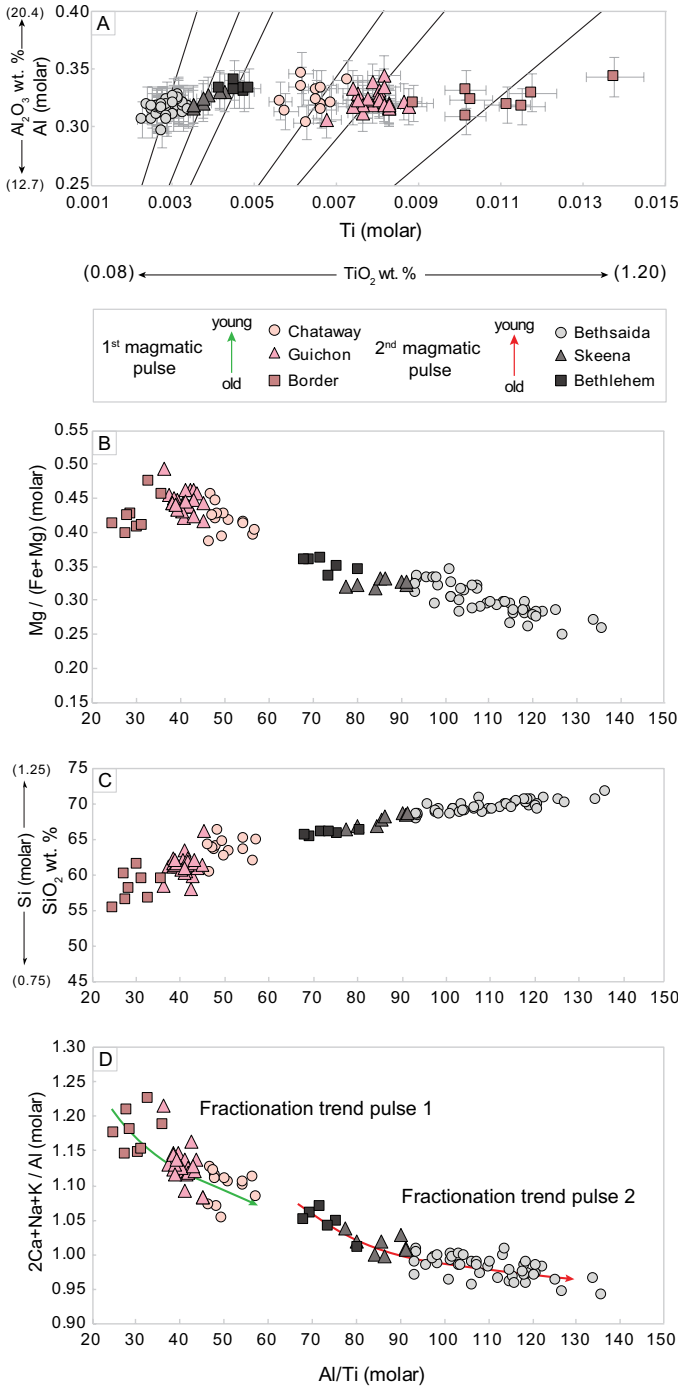

Fig. 4. Least altered host-rock discrimination diagrams. A. Al versus Ti (molar); the analytical error bars shown are 6% of the value. B. Mg/(Mg + Fe) versus Al/Ti. The Guichon Creek batholith magmatic suite evolved toward lower Mg#. C. Si versus Al/Ti. Rocks evolve toward higher Si content through time. D. (2Ca + Na + K)/Al versus Al/Ti. Rocks in the Guichon Creek batholith show two fractionation trends toward decreasing (2Ca + Na + K)/Al associated with each pulse of magmatism. The least altered, or precursor, mean (2Ca + Na + K)/Al values for the host rocks are ~1.20 (Border), 1.12 (Guichon), 1.10 (Chataway), 1.05 (Bethlehem), 1.00 (Skeena), and 0.97 (Bethsaida).

(Fig. 5B). Vein margins are typically irregular and diffuse (Table 1). In albite-bearing halos primary mafic minerals are replaced by chlorite with accessory titanite and lesser actinolite. At Valley-Lornex and Highmont, albite alteration is crosscut by bornite-bearing, quartz-coarse-muscovite veins (Table 1). Calcite veinlets crosscut and refractured epidote-(albite) facies veins (Fig. 6A, B). Around the Valley-Lornex deposits in the Bethsaida unit, the epidote-(albite) facies is crosscut by prehnite and calcite veinlets and is locally overprinted by prehnite-(white-mica–prehnite) propylitic alteration of varying intensity (Table 1).

Domains of epidote veins (>1.25 cm/m) with K-feldspar–destructive albite halos have a nonconcentric distribution in the Guichon Creek batholith (Fig. 2A; Table 1). Wall-rock alteration is generally restricted to within 2 to 3 cm of epidote veins or fractures and occurs in fracture-controlled sodic-calcite domains that extend up to 7 km away from the porphyry centers (Fig. 2). Some isolated domains of sodic-calcic facies occur in mafic Border rocks. If these are excluded the total mapped area of sodic-calcic facies is ~34 km^2.

White mica-chlorite: Quartz-(muscovite) and fine-grained white-mica–chlorite alteration: Quartz-(muscovite) facies comprise coarse-grained (~0.3–1.5 cm) gray muscovite, with a short-wavelength Al-OH feature, which typically occurs in the halos of quartz ± chalcopyrite and bornite veins (e.g., Fig. 5C; Table 1). Pervasive, selectively pervasive, and fracture-controlled fine-grained (<1 mm), white mica with predominantly intermediate-wavelength Al-OH features constitute the white-mica–chlorite alteration assemblage (Table 1; Fig. 5D). Veinlets of Cu-Fe sulfide, and locally specularite, are intimately associated with white-mica–chlorite facies (Table 1). In this paper, quartz-(muscovite) and white-mica–chlorite facies are grouped together as white-mica–chlorite facies because of their mineralogical similarity and close spatial association with the mineralization in the porphyry Cu centers (Table 1). Calcite most commonly occurs as microveinlets with white-mica–chlorite facies but is also locally intergrown with fine-grained white mica, chlorite, and Cu-Fe-sulfide in halos (Figs. 6C, D). Additionally, calcite formed irregular blebs in well mineralized late-stage Cu-rich veins and in white mica and clay-altered fault zones that crosscut main stage Cu mineralization at the porphyry centers (Table 1).

The quartz-(muscovite) facies occurs with the main-stage Cu mineralization at Valley-Lornex and locally at Highmont (Table 1; Fig. 2). White-mica–chlorite ± carbonate alteration occurs with sulfide mineralization at Bethlehem, J.A., and Highmont. It also overprints quartz-(muscovite) vein and halo domains at Valley and Lornex (Table 1; Fig. 2). The distribution of the white-mica–chlorite facies generally is limited to the sulfide-bearing domains within the porphyry Cu centers but is also recognized in narrow (1–10 m) zones at several regional Cu occurrences (Table 1; Fig. 2). Variable amounts of kaolinite and montmorillonite (i.e., intermediate argillic alteration; Table 1) typically overprint relict feldspars outside of the white-mica–chlorite alteration halos and zones at the porphyry centers. Overall, however, kaolinite and montmorillonite are primarily restricted to the porphyry Cu centers and some Cu occurrences.

Propylitic: Epidote-(K-feldspar): This subfacies comprises epidote veins with weakly developed and patchy K-feldspar ±

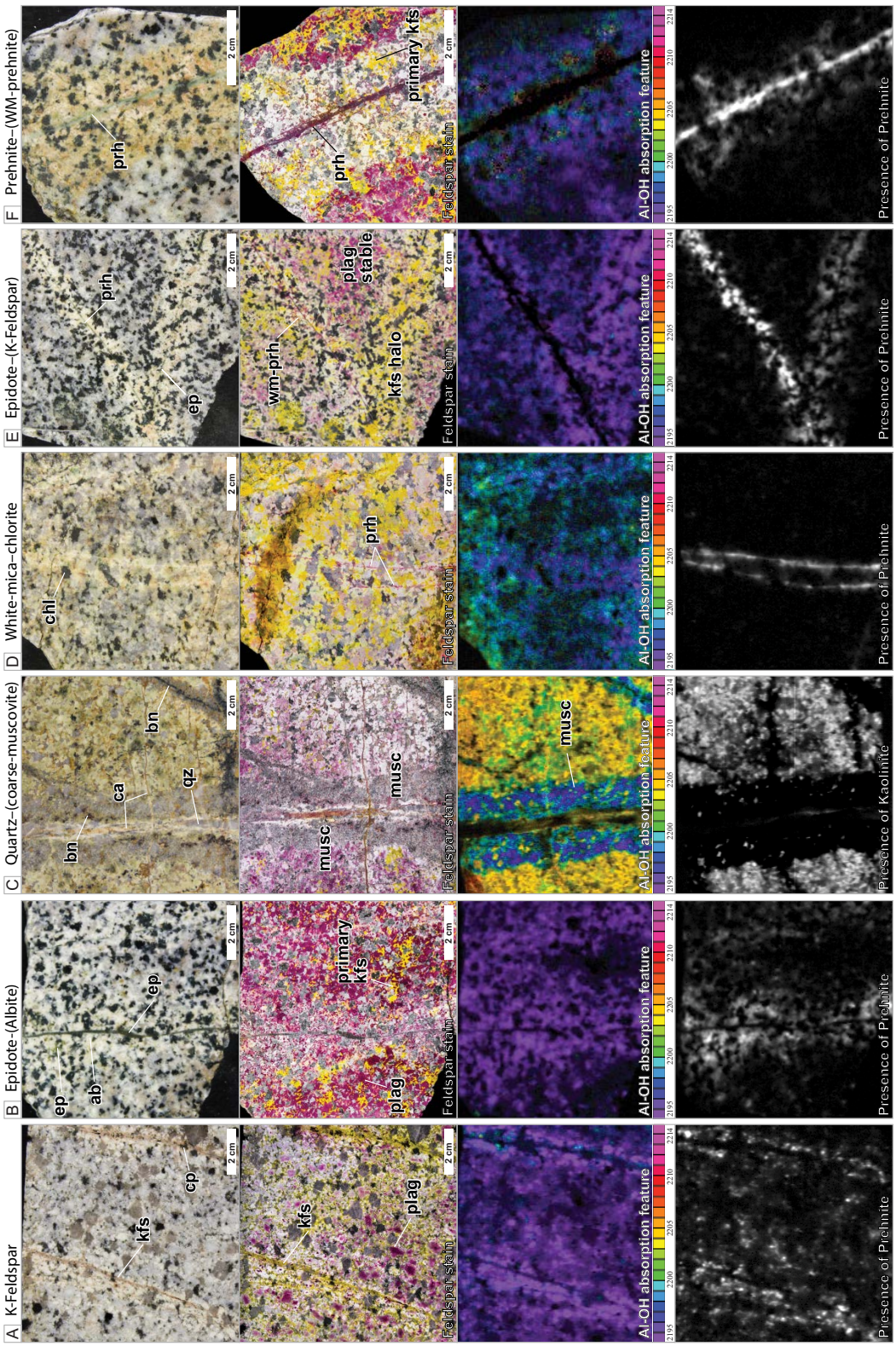

Fig. 5. Examples of the alteration facies in the Guichon Creek batholith. A. K-feldspar fracture halo; potassic. Patchy K-feldspar alteration of plagioclase within halos around fractures with trace chalcopyrite fill. Trace, short-λ white mica and prehnite present throughout. B. Epidote vein with K-feldspar–destructive albite halo and patchy epidote in the plagioclase sites; epidote-(albite), sodic-calcic facies. Note the whitening of the feldspars and the absence of the yellow stain that defines the K-feldspar–destructive albite halo around the epidote vein fill. Trace, short-λ white mica and prehnite also present in the halo. C. Quartz ± bornite veins with diagnostic coarse-grained, gray, muscovite halos; quartz-(muscovite) subfacies of white-mica–chlorite facies. Pervasive trace kaolinite alteration of feldspar results in ineffective staining of the feldspar sites. The coarse muscovite is characterized by short- to intermediate-λ spectral response. D. Pervasive fine-grained white mica-chlorite; white-mica–chlorite facies. K-feldspar is mostly stable, but plagioclase is pervasively altered to fine-grained white mica with intermediate-λ spectral response. Mafic minerals are selectively altered to chlorite. Note the late prehnite veinlets (pink stained). E. Epidote vein with K-feldspar halo; epidote-(K-feldspar) subfacies of propylitic facies. Plagioclase is partially altered to K-feldspar within the halo, whereas mafic minerals are selectively and pervasively altered to chlorite. Note the prehnite veinlet with plagioclase-destructive short-λ white-mica and prehnite halo, which possibly crosscuts the epidote veinlet. F. Prehnite ± pumpellyite veinlet with fine-grained white-mica–prehnite halo; prehnite-(white-mica–prehnite) subfacies of propylitic facies. Note the prehnite veinlet pink stains and the reddening within the alteration halo. K-feldspar is stable, whereas plagioclase has been selectively and incompletely replaced by short-λ white mica and accessory prehnite (small pink-stained grains within the halo). Mineral abbreviations: ab = albite, bn = bornite, ca = calcite, chl = chlorite, cp = chalcopyrite, ep = epidote, kfs = K-feldspar, musc = muscovite, plag = plagioclase, prh = prehnite, qz = quartz, wm = white mica.

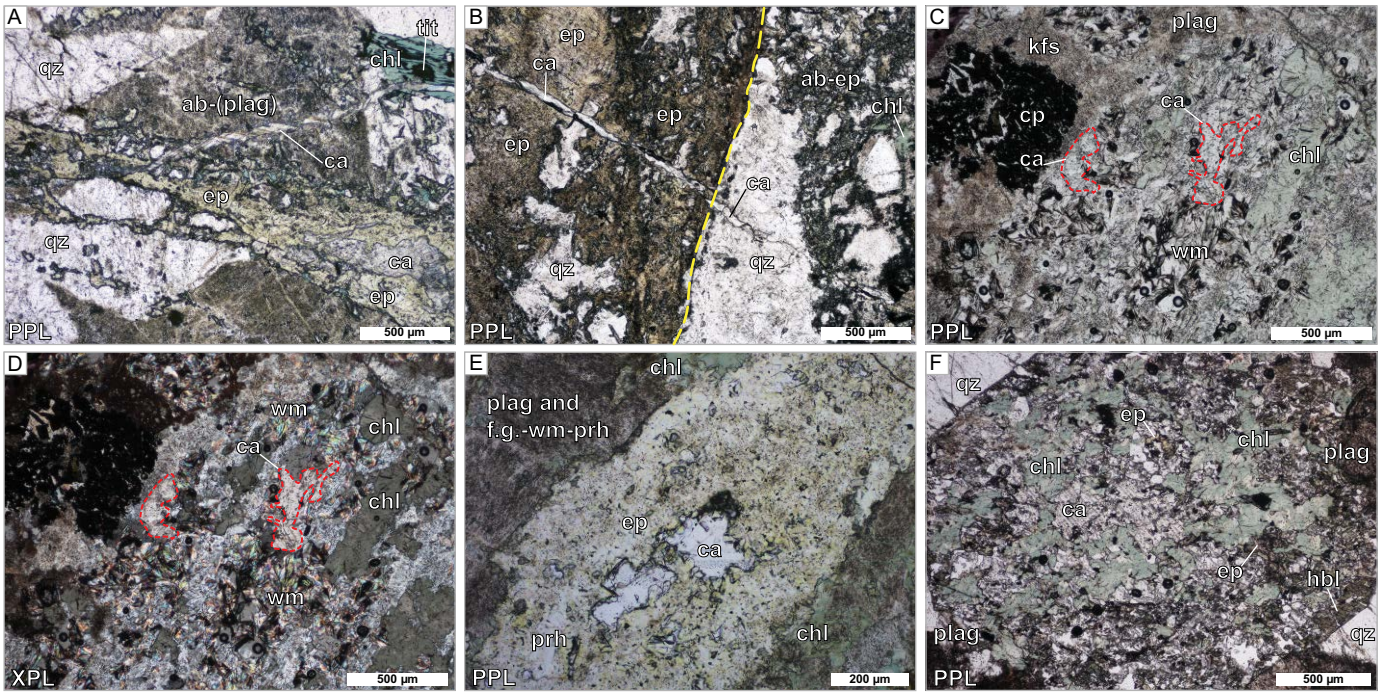

Fig. 6. Photomicrographs of calcite paragenesis in altered rocks. A. Calcite veinlet crosscutting and occluding an epidote vein with an albite and chlorite halo. B. Calcite cutting epidote-(albite) vein. The yellow dashed line indicates the epidote vein wall boundary. C. Calcite intergrown with well-developed white-mica–chlorite alteration and chalcopyrite mineralization associated with white-mica–chlorite alteration facies. D. Cross-polarized light (XPL) view of Figure 6C. E. Calcite occluding an epidote vein with a prehnite-fine-grained white-mica halo associated with prehnite-(prehnite–white-mica) alteration. Note the turbidity of the feldspar in plane-polarized light (PPL) is due to porosity and fine-grained secondary mineral inclusions. F. Hornblende phenocryst replaced by chlorite, calcite, and epidote associated with the prehnite-(prehnite–white-mica) alteration facies. Mineral abbreviations: ab = albite, bn = bornite, ca = calcite, chl = chlorite, cp = chalcopyrite, ep = epidote, f.g. = fine-grained, kfs = K-feldspar, musc = muscovite, plag = plagioclase, prh = prehnite, qz = quartz, tit = titanite, wm = white mica.

epidote halos and results in the selective replacement of mafic minerals by chlorite (Figs. 2B, 5E; Table 1). Primary K-feldspar appears stable within these halos. Minor prehnite occurs intergrown with epidote in some veins, whereas pumpellyite is a late or crosscutting phase. Additionally, some veins exhibit zoned halos of an inner zone of K-feldspar and outer zone of white-mica alteration (predominately after plagioclase). Epidote-(K-feldspar)–altered rocks are restricted to the more mafic host rocks (i.e., the Guichon and Chataway granodiorites) (Fig. 2B).

Propylitic: Prehnite-(white mica-prehnite): Veinlets (~<0.2cm) of prehnite ± epidote and calcite with plagioclase-destructive white-mica–prehnite halos constitute the prehnite-(white-mica–prehnite) subfacies (Fig. 5F). The white mica in the halos of the prehnite ± epidote veins commonly have a short-wavelength Al-OH feature (Table 1). Mafic minerals are weakly to moderately altered to chlorite ± carbonate, prehnite, and vermiculite within the halo, but the host rock is typically unaltered between fractures (Table 1). Calcite infills vug spaces (occludes) in some epidote-prehnite veins (Fig. 6E) and locally replaced hornblende along with chlorite and epidote in prehnite-(white-mica–prehnite) halos (Fig. 6F). Prehnite-(white-mica–prehnite) alteration overprinted epidote-(albite) and locally crosscut mineralized veins of the white-mica–chlorite facies. In the Bethsaida granodiorite, prehnite is more abundant than epidote in veinlets of propylitic facies compared to the other, more mafic host rocks (Fig. 2).

The prehnite-(white-mica–prehnite) facies is the most common and widely distributed alteration in the batholith. The highest density of this vein type is centered around the porphyry Cu centers (Fig. 2A), but veins also occur out to the margins of the batholith (cf. Fig. 2B).

PER, MER, and mobile elements characteristics of altered rocks

The altered samples were organized by host rock to reduce the effects of fractionation-related chemical trends (i.e., Fig. 4) and to improve visualization of the results. The samples are colored by the alteration facies and any overprint present and symbolized hierarchically based on the presence of (1) white-mica–chlorite halos, (2) albite halos, (3) K-feldspar halos, and (4) prehnite-(white-mica–prehnite) halos (Figs. 7–9).

Potassic: K-feldspar: Potassically altered rocks plot on the feldspar control line and overlap with other alteration facies in the (2[Ca-C] + Na + K)/Ti versus Al/Ti diagram (Fig. 7A). In terms of K/Ti versus (Al-2[Ca-C]-Na)/Ti the K-feldspar–altered rocks plot close to or on the K-feldspar control line (Fig. 7B); the data that plot high on the K-feldspar control line contain more K-feldspar than points lower on the K-feldspar control line. Many samples containing K-feldspar alteration overlap with the least altered rock field, but a subset shows K-

feldspar addition. Potassically altered samples that have been overprinted by a white-mica–chlorite assemblage are shifted toward the muscovite control line (Fig. 7B). A few K-feldspar–altered rocks hosted by Guichon and Chataway granodiorite plot above the least altered rock domain and have high Rb/Sr and low Rb/Ba (Fig. 8). In the other host rocks, however, the K-feldspar facies is indistinguishable from the least altered and prehnite-(white-mica–prehnite) facies rocks in terms of Sr-Ba-Rb (Fig. 8). The K-feldspar facies, however, can be discriminated based on elevated Cu concentrations (i.e., >100 ppm in Bethsaida) and, generally, has high K/Th values compared to the least altered rocks (Fig. 9).

Sodic-calcic: Epidote-(albite): Epidote-(albite)–altered rocks mostly plot on the feldspar control line overlapping with the least altered rocks (Fig. 7A). In the Bethsaida granodiorite, however, numerous albite-altered samples are shifted toward the muscovite control line (Fig. 7A). Samples altered by albite plot below the least altered domains on or close to the K-feldspar control line (Fig. 7B). Sodic-calcic facies rocks that have been overprinted by white mica-chlorite plot on the muscovite control lines, but at low K/Ti values (blue-colored X symbol, Fig. 7A, B). The variation in the proportions of K-feldspar, muscovite, and kaolinite in the epidote-(albite) facies in Bethsaida granodiorite at low K/Ti values is evident in Figure 7B. On a plot of K/(Al-2[Ca-C]) versus Na/(Al-2[Ca-C]), i.e., with compositions projected from anorthite, the epidote-(albite)–altered Bethsaida granodiorite is shifted toward the albite

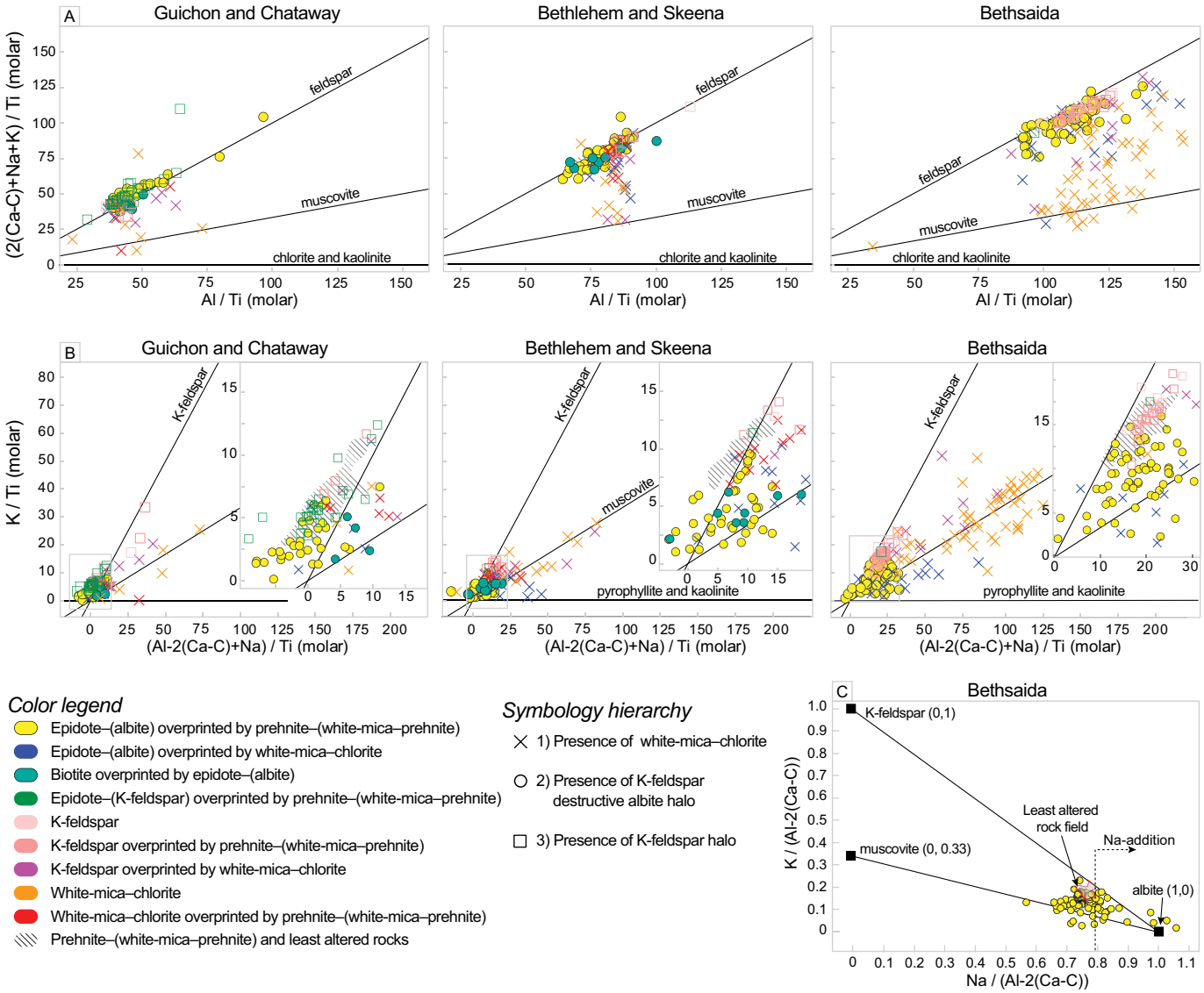

Fig. 7. Pearce element ratio and general element ratio diagrams for Guichon and Chataway, Bethlehem and Skeena, and Bethsaida host rocks. A. (2[Ca-C] + Na + K)/Ti versus Al/Ti, in which the [Ca-C] term adjusts for the Ca in calcite. Mineral control lines are indicated for feldspar, muscovite, and chlorite-kaolinite. B. K/Ti versus (Al-2[Ca-C]-Na)/Ti. Mineral control lines shown for K-feldspar, muscovite, and pyrophyllite and kaolinite (projected from anorthite and albite). Insets show detail from the region of the diagrams highlighted with the gray rectangle. C. Epidote-(albite) samples (sodic-calcic) plotted in Na/(Al-2[Ca-C] versus K/(Al-2[Ca-C]) space (projected from anorthite). Field for least altered Bethsaida granodiorite shown.

node relative to the least altered rock field (Fig. 7C). Approximately 30% of the epidote-(albite)–altered samples in Bethsaida granodiorite exhibit Na addition, and numerous samples of this facies are situated on the albite-muscovite tie line (Fig. 7C). Albite-altered rocks form arrays in Sr-Ba-Rb space that extend from least altered host-rock compositions toward high Sr/Ba and low Rb/Sr (Fig. 8). Similarly, albite-altered rocks that were overprinted by white mica-chlorite plot in the same field as the epidote-(albite) facies. The high Sr/Ba response corresponds to samples with low K/Al and high Na/Al. Epidote-(albite) facies rocks exhibit a wide range of K/Th that partially overlaps with the least altered rocks, but overall they have lower K/Th and Cu contents (Fig. 9).

White mica-chlorite: Samples identified as white-mica–chlorite–altered plot between the feldspar and muscovite control lines, where the slope of the line between the datum and the origin corresponds directly to the amount of white mica in the sample (Fig. 7A). The white-mica–chlorite facies rocks have a wide range of K/Ti values that plot along the muscovite control line (Fig. 7B); samples with high K/Ti on the control line are mostly quartz-(muscovite) veins and halos from the Valley pit. There appears to be substantial K, Ca, and Na transfer associated with some white-mica–prehnite alteration. Rocks affected by white-mica–prehnite alteration have higher Rb/Sr and higher Rb/Ba than least altered and prehnite-(white-mica–prehnite) altered rocks (Fig. 8). This facies can be further distinguished by elevated K/Th (Fig. 9).

Propylitic: Epidote-(K-feldspar) and prehnite-(white mica-prehnite): Propylitically altered rocks predominantly plot on or close to the feldspar control line (Fig. 7A). The compositional changes associated with the propylitic subfacies are within the range of the natural variability for K, Na, and Ca, and background white-mica content in each protolith (Fig. 7; Table 2). In terms of Rb-Sr-Ba concentrations, the propylitic subfacies are mostly indistinguishable from the other alteration facies (Fig. 8), though a few samples have high Sr/Ba and low Rb/Sr. Similarly, the propylitic subfacies cannot be discriminated from the least altered rocks based on K/Th value (Fig. 9). A few samples of prehnite-(white-mica–prehnite) alteration, however, do have elevated Cu concentrations and high K/Th relative to the least altered domain and sodic-calcic–altered rocks (Fig. 9).

Volatile (H_2O-OH and CO_2) characteristics of altered rocks

By plotting the molar ratios of Ca/Ti against CO_2/Ti, the composition of carbonate present in the whole-rock samples can be estimated (Fig. 10A). Most Guichon Creek batholith samples plot close to the anorthite, prehnite, and epidote trend line, but some extend toward, and form an array along, the calcite control line. Samples with a slope between vertical

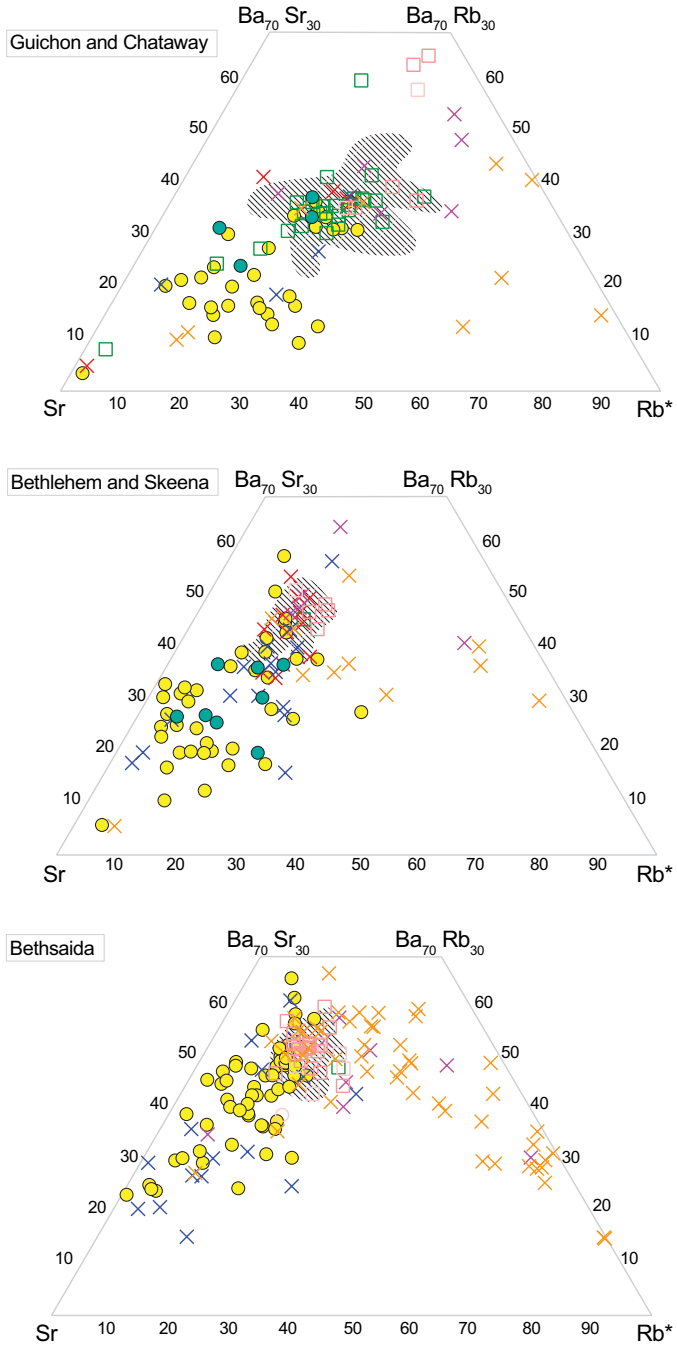

Fig. 8. Strontium-Ba-Rb ternary diagrams for Guichon and Chataway, Bethlehem and Skeena, and Bethsaida host rocks. Albite-altered rocks show a shift toward high Sr/Ba and Sr/Rb, whereas rocks with white-mica–chlorite alteration have high Rb/Ba and low Sr/Rb. Prehnite-(prehnite-white mica) and least altered rocks, and most K-feldspar–altered rocks, plot in the same location within the Sr-Ba-Rb ternary system, per host-rock group. Albite-altered rocks overprinted by white mica-chlorite have a range of values but appear to preserve a high Sr/Ba signature.

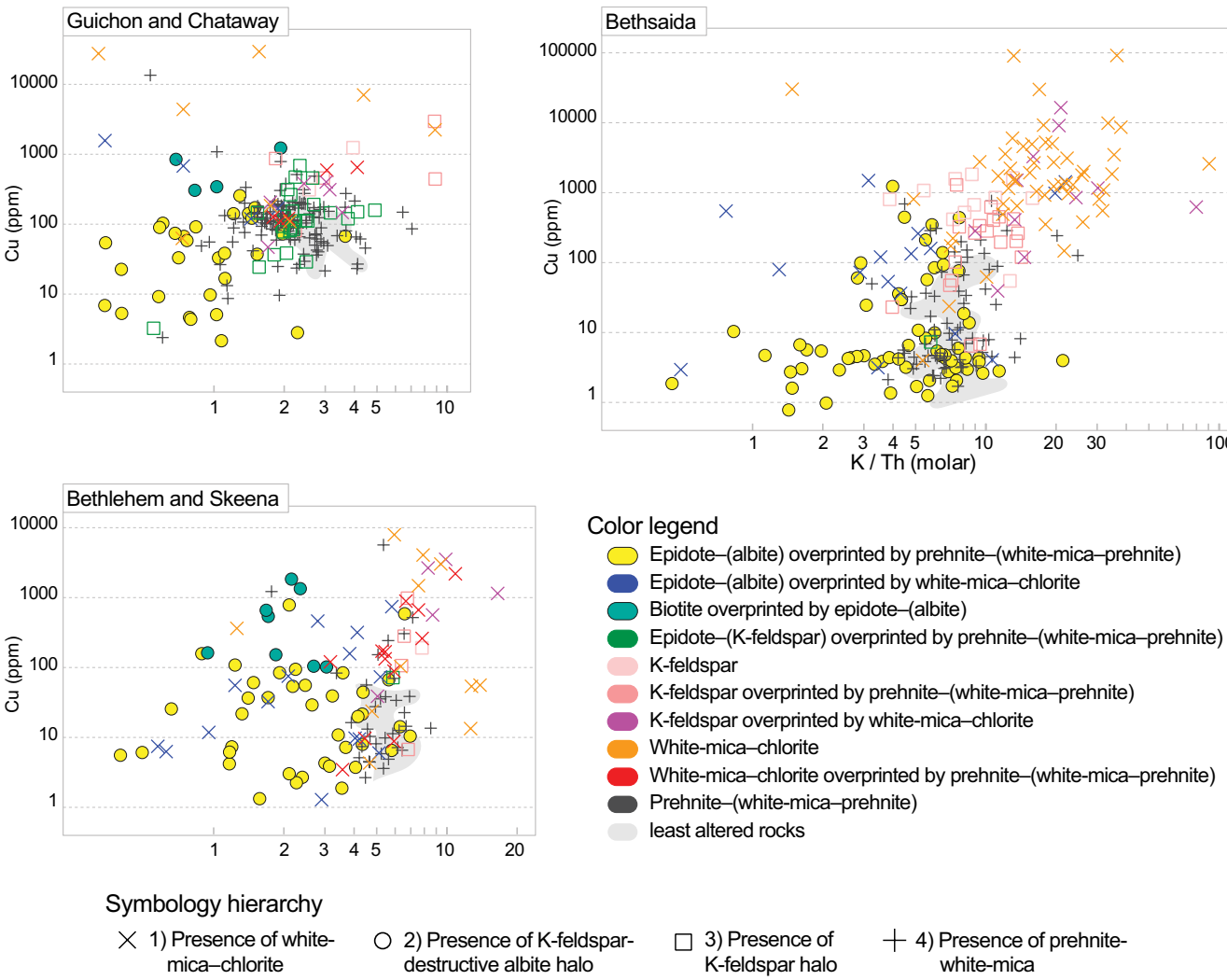

Fig. 9. Copper concentrations versus K/Th for Guichon and Chataway, Bethlehem and Skeena, and Bethsaida host rocks. The epidote-(K-feldspar) alteration facies is predominantly associated with the more mafic host rocks (Guichon and Chataway) and is not elevated in Cu or K/Th relative to least altered rocks, and prehnite-(white-mica–prehnite) facies. K-feldspar alteration facies in Bethsaida partially overlaps with the least altered and prehnite-(prehnite–white-mica) field but some samples extend toward higher K/Th and correspond to samples with high K/Ti in Figure 7B. Additionally, rocks with K-feldspar halos and no epidote vein fill are distinguished by elevated Cu contents. White-mica–chlorite–altered samples have high K/Th and generally higher Cu than the other facies, the inverse is true for epidote-(albite) facies in each host rock.

and 1 contain some carbonate that is interpreted to be calcite; this is supported by electron probe microanalysis results (App. 2).

Calculated H_2O-OH and CO_2 concentrations generally increase together in the altered Skeena and Bethsaida granodiorites that host the Valley-Lornex and Highmont porphyry systems (Fig. 10B). The least altered Skeena and Bethsaida granodiorite samples predominantly contain <0.04% CO_2 and have H_2O-OH values ranging between 0.25 and ~1.75 wt % (Fig. 10B). Numerous sodic-calcic samples plot within the least altered rock field (Fig. 10). A subset of epidote-(albite)–altered rocks extend to higher values of CO_2, H_2O-OH, and to (2[Ca-C] + Na + K)/Al values <0.9 (Fig. 10B). Samples with (2[Ca-C] + Na + K)/Al values <0.85 are predominantly associated with white-mica–chlorite halos and CO_2 and H_2O-OH in excess of ~0.45 and 1.0 wt %, respectively (Fig. 10B). The prehnite-(white-mica–prehnite) propylitic subfacies have calculated H_2O and CO_2 contents like least altered rock compositions, but, critically, a subset of samples extends to higher values of both CO_2 and H_2O-OH and has (2[Ca-C] + Na + K)/Al values of 0.9 to 0.85 (Fig. 10).

The $\delta^{18}O$ and $\delta^{13}C$ values of carbonate from 30 whole-rock pulps are reported in Table 3. Four least altered rock samples contained carbonate below the detection limits of the analytical technique. Carbonate from altered rocks in the Guichon Creek batholith has $\delta^{18}O$ values between 9.5 and 19.2‰ with an average value of 13.1‰, and $\delta^{13}C$ values that range from –7.5 to –1.6‰, with an average value of –4‰. No systematic variation in carbonate isotope composition with respect to alteration facies is evident (Table 3).

Material transfer

Isocon diagrams of altered and fresh granodiorite have Al_2O_3, TiO_2, P_2O_5, and Zr concentrations with constant ratios and

that form a line that projects back to the origin, indicating that these elements were immobile during alteration (Fig. 11; App. 4). Zirconium concentrations are more variable in the mafic host rocks than in the felsic units, i.e., they are less conserved with respect to magmatic processes (Table 2). Additionally, the concentration of TiO_2 (and mafic minerals) in the least altered host rocks is low (<1%) and more variable than the concentration of Al_2O_3 (Table 2). Consequently, we elected to use Al_2O_3 in material transfer (element gain and loss) calculations, consistent with the methods outlined by Grant (1986). Here, the material transfer of the major oxides is expressed as a percent change from the least altered rock median values, and the other elements are in parts per million. Material changes greater than 1 standard deviation of the least altered rock suite are considered to be significant (Table 4). Figure 12 shows the median response for the major oxides, volatiles, and select minor elements per alteration facies for all samples hosted by the Guichon (mafic) and Bethsaida (felsic) granodiorites (Table 4).

In the Guichon granodiorite isocon plot, the sodic-calcic alteration is highly depleted in Fe_2O_3, K_2O, Ag, Au, Ba, Rb, and Li, is moderately depleted in Cu, Co, Fe_2O_3, Ni, and Pb, and has a minor depletion in MgO, Ce, and Sr concentrations (Fig. 11A). Conversely, Na_2O, CaO, Mn, Zn, and H_2O-OH are rich in the sodic-calcic–altered sample relative to the least altered values (Fig. 11A). The element changes in sodic-calcic alteration hosted in Guichon granodiorite shown on the isocon plot (Fig. 11A) are confirmed by the strong depletion in K_2O (–32%) and Ba (–260 ppm) and enrichments in CaO (11%), Na_2O (4%), and Mn (30 ppm) in the Bethsaida granodiorite shown in Figure 12. More significant enrichment in CaO (18.5%) and Na_2O (8.2%) locally occurred with sodic-calcic alteration, as evidence by the 75th percentile values of the sample suite (Table 4; Fig. 12). The mafic host rock, the Guichon granodio-

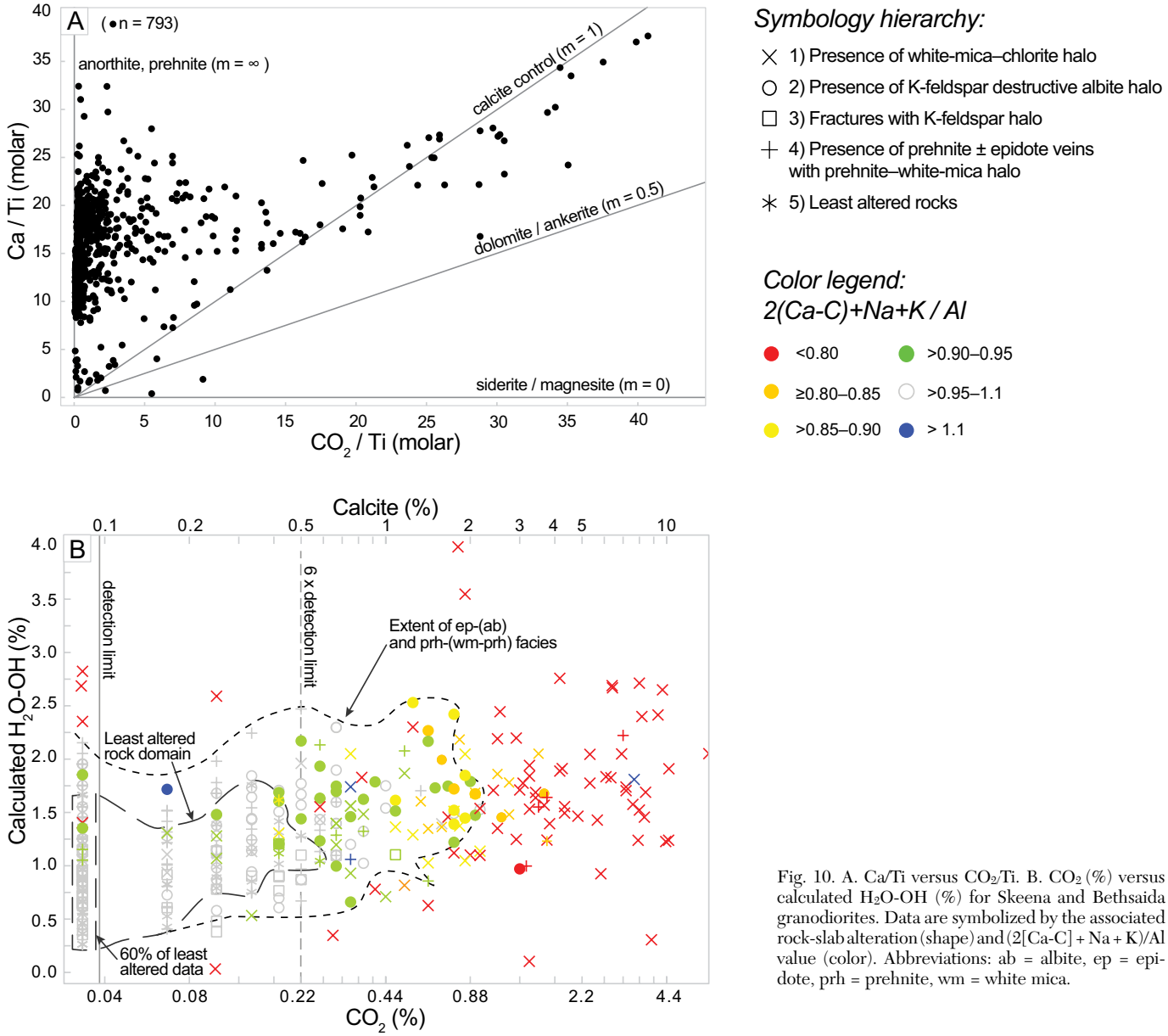

Fig. 10. A. Ca/Ti versus CO_2/Ti. B. CO_2 (%) versus calculated H_2O-OH (%) for Skeena and Bethsaida granodiorites. Data are symbolized by the associated rock-slab alteration (shape) and (2[Ca-C] + Na + K)/Al value (color). Abbreviations: ab = albite, ep = epidote, prh = prehnite, wm = white mica.

Table 3. The $\delta^{18}O$ and $\delta^{13}C$ Values of Carbonate from Whole-Rock Pulps

Sample	Rock type	Al/Ti	Alteration facies	LOI (%)	S (%)	CO_2 (%)	H_2O-OH (%)	Cu (ppm)	K/Ti	(2[Ca-C] + Na + K)/Al	$\delta^{13}C$ (‰ vs. VPDB)	$\delta^{18}O$ (‰ vs. VSMOW)
2238992	Bethsaida	118	Ep-(ab)	1.4	0.01	0.04	1.4	1.9	0.89	1.03	–4.4	16.2
2238999	Bethsaida	107	Ep-(ab)	2.1	0.01	0.48	1.6	3.9	7.00	0.87	–3.2	11.7
2242914	Skeena	80	Ep-(ab)	3.1	0.02	0.55	2.5	55.7	2.65	0.86	–7.5	13.6
2245428	Chataway	51	Ep-(ab)	1.1	0.01	0.22	0.9	9.7	3.11	1.11	–4.0	12.9
2245439	Chataway	60	Ep-(ab)	2.5	0.01	0.55	1.9	2.2	3.79	1.06	–4.1	10.7
2245488	Skeena	84	Ep-(ab)	1.3	0.01	0.04	1.3	3.0	3.50	1.03	–5.7	16.6
2247904	Bethsaida	116	Ep-(ab)	1.6	0.01	0.11	1.5	4.8	10.09	0.89	–4.3	13.4
2247931	Bethsaida	93	Ep-(ab)	1.8	0.01	0.33	1.5	2.7	3.89	0.93	–3.8	13.9
2247936	Skeena	89	Ep-(ab)	2.0	0.01	0.37	1.6	3.7	6.72	0.92	–5.2	10.8
2758873	Bethsaida	105	Ep-(ab)	2.3	0.01	0.84	1.4	4.3	8.84	0.83	–3.7	12.2
2232412	Bethsaida	92	Ep-(ab) ovrp. wm-ch	3.8	0.08	1.83	1.9	79.2	4.47	0.65	–2.0	15.7
2242933	Dike	206	Ep-(ab) ovrp. wm-ch	1.9	0.03	0.95	0.9	666.5	16.27	0.71	–3.0	11.5
2245458	Skeena	84	Ep-(ab) ovrp. wm-ch	3.0	0.01	0.81	2.2	157.7	8.76	0.82	–6.1	11.9
2247950	Bethsaida	110	Ep-(ab) ovrp. wm-ch	2.9	0.01	0.84	2.0	133.7	10.48	0.84	–2.9	10.9
2245456	Skeena	81	Wm-ch	1.3	0.03	0.04	1.2	890.0	10.01	0.99	–2.4	10.6
2247946	Bethsaida	96	Wm-ch	2.9	0.01	0.62	2.3	510.1	8.93	0.85	–2.8	13.2
2238993	Bethsaida	112	Prh-ep-pump	0.8	0.01	0.04	0.8	46.7	16.25	0.96	–2.2	19.2
2247938	Bethsaida	99	Prh-ep-pump	1.2	0.01	0.04	1.2	191.6	11.86	0.99	–6.3	14.2
2242906	Skeena	88	Prh-ep-pump	1.6	0.02	0.29	1.3	13.6	12.10	0.95	–2.3	11.7
2245375	Border	24	Prh-ep-pump	3.1	0.27	0.33	2.5	3,733.1	0.82	1.19	–1.6	11.4
2245418	Chataway	47	Prh-ep-pump	1.5	0.01	0.18	1.3	65.6	8.21	1.04	–3.2	9.5
2245424	Chataway	51	Prh-ep-pump	1.7	0.01	0.18	1.5	49.5	7.33	0.98	–5.4	14.4
2245433	Skeena	83	Prh-ep-pump	1.6	0.01	0.04	1.6	11.3	9.07	1.02	–5.4	14.1
2245452	Skeena	86	Prh-ep-pump	1.9	0.01	0.11	1.8	152.5	9.58	0.95	–3.1	15.3
2758859	Bethsaida	93	Prh-ep-pump	1.9	0.01	0.29	1.6	4.3	12.87	0.99	–4.2	12.7
2758890	Bethsaida	109	Prh-ep-pump	2.3	0.01	0.59	1.7	10.9	17.87	0.93	–4.2	11.2
2758897	Bethsaida	108	Prh-ep-pump	2.0	0.01	0.04	2.0	36.5	14.07	1.04	-	-
2758855	Bethsaida	93	Prh-ep-pump	1.5	0.01	0.04	1.5	690.5	10.69	1.00	-	-
2242901	Guichon	39	Prh-ep-pump	1.9	0.01	0.04	1.9	9.61	3.08	1.18	-	-
2245387	Chataway	48	Ep-(kfs)	1.1	0.01	0.04	1.1	471.8	12.38	1.04	-	-

C% detection limit by LECO is 0.01 ~= 0.04% CO_2 and 0.08 calcite equivalents; dashes indicate samples were below detection limit

Abbreviations: ab = albite, ch = chlorite, ep = epidote, kfs = K-feldspar, ovrp. = overprint, prh = prehnite, pump = pumpellyite, VPBD = Vienna Pee Dee Belemnite, VSMOW = Vienna standard mean ocean water, wm = white mica

rite, is more depleted in Fe_2O_3 (–9%), Ba (–440 ppm), and Cu (–65 ppm) and possibly Zn (25th percentile = –11 ppm) relative to concentrations of these elements in more felsic Bethsaida granodiorite. No significant changes in SiO_2 concentrations occurred with epidote-(albite) alteration. Both host rocks show significant addition of CO_2 (533–643%) and H_2O-OH (74–89%) during sodic-calcic alteration (Fig. 12).

Potassic alteration in Bethsaida granodiorite is enriched in K_2O (15%) and depleted in CaO (–6%), but the latter is within 1 standard deviation of the least altered sample suite. Concomitant depletion of CaO with enrichment in K_2O, however, is indicated by the 25th percentile value of CaO change in the potassically altered sample suite (Table 4). Depletion of CaO is more pronounced in the Guichon than in the Bethsaida granodiorite (Fig. 12). K-feldspar–altered rocks are strongly enriched in copper (Fig 12), and depletion in Mn may be occurring in Bethsaida granodiorite (see next section), but generally it is within the natural variation for this host rock. The potassic facies is not significantly enriched in CO_2 and H_2O-OH.

Sample 2014GL173 (Fig. 5C) is an example of a white-mica–chlorite facies rock hosted in the Skeena granodiorite (Fig. 11B). This quartz-(muscovite) subfacies sample is strongly enriched in Cu, Ag, W, Bi, Mo, CO_2, Au, Pb, Sb, As, and H_2O-OH and is weakly enriched in Rb, SiO_2, and K_2O (Table 4; Fig 11B). The coarse muscovite-altered sample is strongly depleted in calcium oxide and Ba and moderately depleted in Sr, Zn, Li, and Na_2O (Fig. 11B). The white-mica–chlorite facies, hosted in the Bethsaida granodiorite, are consistently enriched in SiO_2 (9%), K_2O (90%), and Cu (1,876 ppm) and depleted in CaO (–11%), Na_2O (–49%), and Sr (–267 ppm). Both host rocks have had a significant addition of volatiles during white-mica–chlorite alteration (Fig. 12), but the Bethsaida granodiorite, host rock to the Valley-Lornex porphyry, is particularly enriched in CO_2 (4,396%) and H_2O-OH (125%).

No significant changes in the major oxides are associated with either of the subfacies of propylitic alteration, but both are enriched in H_2O-OH (41–56%) relative to the least altered sample suite. A wide range of enrichment in CO_2 characterizes the prehnite-(white-mica–prehnite) propylitic subfacies (Table 4).

Spatial distribution of alteration intensity and material transfer

In order to compare the intensity of the feldspar-destructive white-mica alteration between the different district-scale host rocks in the Guichon Creek batholith, the (2[Ca-C] + Na + K)/Al value for each sample was normalized to its least altered equivalent host rock. The delta values (Δ) between the least altered host rock (2Ca + Na + K)/Al value (Fig. 4D) and 1 (the feldspar control line) were subtracted from the measured (2[Ca-C] + Na + K)/Al value for each sample.

The porphyry Cu centers exhibit moderate to intense white-mica alteration (i.e., (2[Ca-C] + Na + K)/Al values of

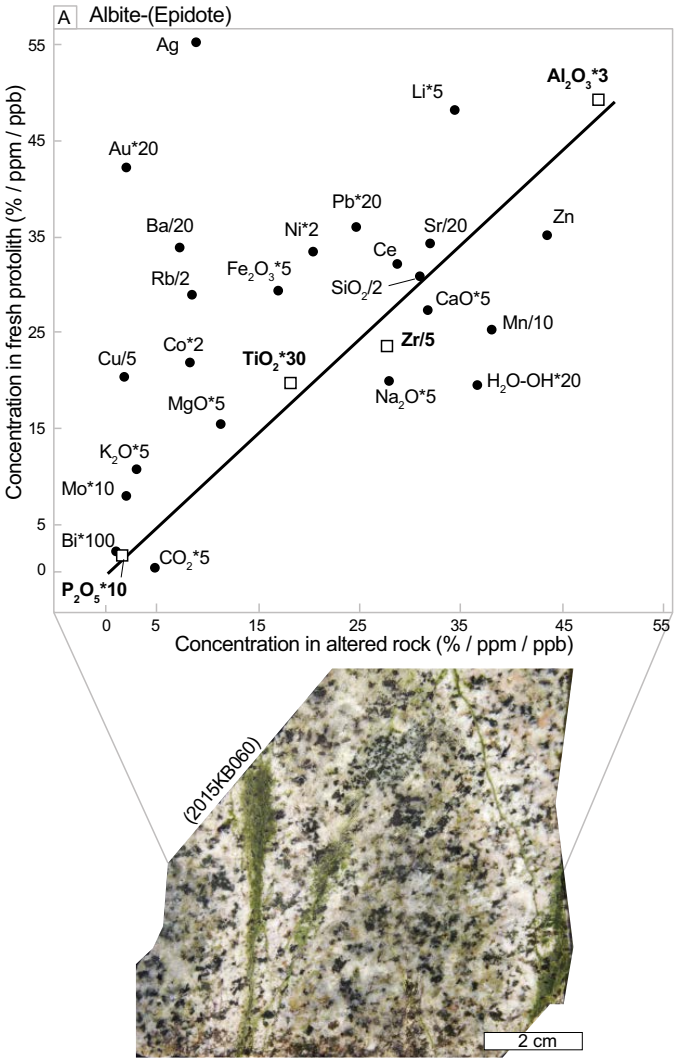

Fig. 11. Isocon diagrams with selected and weighted elements in which the protolith versus the altered samples are plotted (after Grant, 1986). A. Epidote-(albite)–altered Guichon (sample 2015KB60 shown). B. White-mica–chlorite facies Skeena (sample 2014GL173 in Fig. 5C). Elements plotting above the isocon line are poor in the altered rock, whereas elements below the line are rich relative to the protolith.

<0.8), show enrichment in K_2O and Cu, and are heterogeneously depleted in Na_2O (Figs. 13, 14) and CaO. Mineralization at the Valley deposit is characterized by >30% increase in K_2O relative to the least altered Bethsaida granodiorite, whereas the response at Lornex and Highmont is more mixed, possibly due to the presence of albite alteration. Sodic-calcic domains are primarily characterized by depletion in K_2O with some addition of Na_2O (Fig. 13) ± CaO. A ~1-km-wide domain west and southwest of the Valley Cu center, with and without white-mica formation, has locally elevated K_2O concentrations (and SiO_2 to a lesser degree). This domain is also weakly to moderately enriched in Cu and appears to be locally depleted in Mn (Fig. 14). For approximately 5 km south of Lornex and Highmont, depletion in K_2O is recorded in some samples within the mapped sodic-calcic domain, and weak white-mica alteration occurs proximal to interpreted structures, but overall the footprint in this area is heterogeneous. Potassium addition also occurred in the rocks south of Lornex at the southernmost fringes of the mapped sodic-calcic domain. White-mica alteration, without SiO_2 but with Mn addition, can be discerned in rocks up to 1 km northeast of Bethlehem (Figs. 13, 14).

Transfer of K_2O and Cu to the host rock and low values of (2[Ca-C] + Na + K)/Al are found at several regional Cu occurrences (Figs. 13, 14). The cluster of samples depleted in K_2O west of the Kathleen Cu occurrence (Fig. 13) do not appear to be albite altered (based on feldspar staining) and are interpreted to be a false negative caused by lower initial K_2O concentrations in the host rock in this area compared to the least altered median value used in the mass transfer calculations.

The addition of CO_2 during alteration occurs throughout the batholith, but the highest density of rocks significantly enriched in CO_2 is within ~3 km of the porphyry centers (Fig. 15). Similarly, a higher proportion of samples enriched in H_2O-OH occurs near the porphyry centers (Fig. 15). An alternative method to investigate enrichment in H_2O-OH is to use Mg (molar) as a denominator; this has the effect of normalizing the data to its mafic mineral content, because mafic minerals are the primary source of water and hydroxyl in least altered rocks. Combining a H_2O-OH/Mg–normalized term with the change in CO_2 concentration enhances the pattern of volatile enrichment. For ~6 km south of Lornex, 2 km southwest of Valley, 0.5 km northeast of Bethlehem, and to a lesser degree 1 km northeast of Highmont, rocks are variably enriched in H_2O-OH and CO_2 (Fig. 15). These areas mostly overlap with the domains of mapped propylitic and sodic-calcic alteration around the porphyry centers.

Discussion

Host-rock control on altered rock mineralogy and composition

The ability to predict alteration products and chemical changes during fluid-rock interaction is important for rec-

Table 4. Summary of Material Transfer Associated with Vein and Alteration Facies in Bethsaida and Guichon Granodiorite

Rock type	Facies	Statistic type	Change (in %) relative to least altered median value (eq. 1)								Change (in ppm) relative to least altered median value					
			SiO_2	Fe_2O_3	MgO	CaO	Na_2O	K_2O	CO_2	H_2O-OH	Ba	Sr	Cu	Pb	Mn	Zn
Bethsaida	Least altered (n = 45)	Mean	0.5	0.8	1.9	2.0	–0.2	2.6	49	26	21	–7	17	0.1	5	0
		Median	0.2	0.2	–0.2	1.9	0.4	–0.1	4	10	3	4	0	0.0	2	0
		Standard deviation	2.5	7.6	13.4	6.9	3.2	12.2	94	29	124	46	41	0.5	56	6
		25th percentile	–0.6	–2.6	–6.2	–3.4	–1.2	–4.3	4	10	–56	–25	–4	–0.1	–28	–5
		75th percentile	1.9	5.0	6.9	5.6	1.8	7.4	8	35	90	21	15	0.3	51	4
	Epidote-(albite) (n = 65)	Mean	1.1	–0.6	6.4	9.1	4.3	–36.3	985	93	–251	47	50	1.1	7	5
		Median	1.2	–0.2	4.5	11.0	4.3	–31.9	643	89	–260	45	–2	0.8	30	5
		Standard deviation	3.6	15.3	13.3	15.3	6.6	24.8	1,021	42	275	128	187	1.6	87	10
		25th percentile	–1.3	–3.8	–2.9	–3.7	0.4	–53.3	264	70	–471	–40	–5	0.4	–65	–1
		75th percentile	3.4	8.4	14.8	18.5	8.2	–17.0	1,505	121	–103	116	10	1.3	68	9
	K-feldspar (n = 30)	Mean	3.2	–4.9	–1.4	–5.8	0.5	17.1	203	17	57	–20	526	0.2	–40	–5
		Median	2.7	–3.3	–1.5	–5.6	0.6	14.8	10	10	72	–17	374	0.1	–41	–5
		Standard deviation	4.4	8.9	8.9	7.1	3.2	19.7	315	13	149	38	518	0.4	51	4
		25th percentile	1.8	–10.2	–6.5	–10.7	–1.7	4.2	6	10	–55	–48	114	–0.1	–76	–7
		75th percentile	3.8	3.4	4.7	–1.1	2.5	23.7	354	21	136	9	773	0.3	4	–2
	White mica–chlorite (n = 61)	Mean	361.1	265.0	–8.6	3.9	–50.3	103.2	5,674	164	–24	–145	9,316	60.5	337	9
		Median	8.9	3.1	–19.3	–11.5	–49.0	90.2	4,396	125	53	–267	1,876	1.2	50	–5
		Standard deviation	2,507.5	1,969.3	90.4	90.5	39.4	86.7	6,760	173	329	588	33,876	459.0	895	81
		25th percentile	3.3	–10.7	–27.1	–23.8	–94.9	39.7	1,564	62	–257	–495	656	0.4	–56	–10
		75th percentile	35.5	37.9	–8.8	22.0	–9.4	171.2	8,129	216	215	–3	5,445	2.1	323	4
	Prehnite-(white mica–prehnite) (n = 71)	Mean	0.3	1.4	3.6	4.3	–0.6	0.1	551	66	–74	–16	66	1.0	17	3
		Median	0.1	1.5	2.1	3.2	0.5	–1.6	8	56	–54	–6	3	0.8	21	2
		Standard deviation	3.2	11.2	17.6	11.9	8.0	15.4	1,482	46	176	74	152	1.0	63	8
		25th percentile	–1.4	–1.8	–3.3	–2.0	–1.8	–8.4	5	27	–172	–45	–3	0.2	–12	–2
		75th percentile	1.8	5.4	12.4	8.6	2.1	11.1	329	104	43	28	68	1.5	56	9
Guichon	Least altered (n = 26)	Mean	–0.6	–0.7	1.1	2.0	0.2	–2.1	60	21	–8	–9	1	0.8	3	4
		Median	–0.1	0.1	0.8	1.0	–0.6	–0.1	5	10	5	–3	0	0.0	4	0
		Standard deviation	4.6	5.9	11.7	7.2	3.6	13.2	83	17	64	42	48	2.9	19	10
		25th percentile	–3.6	–3.8	–4.9	–1.9	–2.6	–9.7	4	10	–33	–38	–34	–1.5	–11	–3
		75th percentile	1.6	2.7	6.7	5.3	2.7	6.7	113	39	39	24	31	2.5	14	12
	Epidote-(albite) (n = 18)	Mean	2.3	–12.4	–8.8	8.4	14.8	–52.6	906	77	–371	11	–58	–0.3	86	0
		Median	1.8	–8.7	–5.7	10.3	8.7	–61.2	533	74	–440	–7	–65	–1.2	75	–1
		Standard deviation	5.0	30.0	13.5	15.9	16.5	27.8	947	48	202	72	68	2.6	150	18
		25th percentile	–1.2	–28.9	–20.0	–7.2	5.3	–74.4	185	36	–530	–40	–119	–1.5	–44	–11
		75th percentile	6.3	4.8	–1.8	20.0	29.2	–27.6	1,768	98	–186	82	–25	0.1	225	7
	K-feldspar (n = 5)	Mean	2.5	42.9	–7.7	–34.1	–18.0	87.1	51	35	606	–152	946	–1.1	11	–7
		Median	3.7	10.0	–11.3	–14.7	–1.4	29.8	9	43	133	–142	335	–1.2	22	–8
		Standard deviation	3.4	66.2	6.6	39.6	33.0	110.6	60	25	821	154	1,281	0.5	26	6
		25th percentile	–0.5	–8.3	–12.3	–76.5	–51.2	–1.1	6	10	–1	–307	68	–1.5	–17	–13
		75th percentile	5.0	110.6	–1.4	–1.3	6.9	204.0	116	57	1,449	–2	2,130	–0.7	33	–1
	White mica–chlorite (n = 13)	Mean	–3.1	51.6	0.5	–13.1	–15.5	–19.8	1,596	69	–231	–82	2,710	0.2	234	21
		Median	–3.8	–1.0	–6.4	–8.0	–6.5	–13.2	524	72	–91	–33	50	–0.8	123	2
		Standard deviation	14.0	127.6	23.1	45.2	34.2	49.8	2,599	46	316	180	8,290	2.3	368	43
		25th percentile	–10.8	–6.6	–9.1	–28.5	–25.3	–66.0	305	27	–528	–191	–17	–1.4	–11	0
		75th percentile	2.7	38.1	5.1	–4.7	0.7	8.2	1,843	111	32	–3	1,516	2.1	302	32
	Prehnite-(white mica–prehnite) (n = 70)	Mean	0.2	1.3	–2.0	0.6	1.2	–5.5	261	50	–43	–2	19	0.2	64	4
		Median	0.2	0.3	–0.5	0.5	0.9	–6.0	10	41	–31	–1	–12	–0.9	40	0
		Standard deviation	7.4	10.5	12.6	13.0	8.0	27.9	500	43	204	104	143	2.8	101	13
		25th percentile	–4.3	–3.2	–7.7	–6.4	–1.5	–18.6	4	10	–165	–63	–43	–1.4	0	–4
		75th percentile	5.2	3.8	5.6	7.2	5.9	12.0	297	64	43	40	45	1	105	9
	Epidote-(K-feldspar) (n = 17)	Mean	–3.2	1.0	0.6	5.8	0.9	–12.4	472	55	–10	8	47	0	75	5
		Median	–2.7	–0.6	3.2	2.3	–0.3	–11.6	10	50	–69	–2	0	–1	42	3
		Standard deviation	5.3	6.9	10.4	16.5	5.2	17.9	935	40	269	108	148	5	86	11
		25th percentile	–5.2	–3.0	–2.6	–2.3	–2.8	–23.8	3	11	–148	–39	–37	–2	15	–1
		75th percentile	–0.7	3.5	6.9	8.4	5.0	0.7	465	93	29	36	44	0	129	8

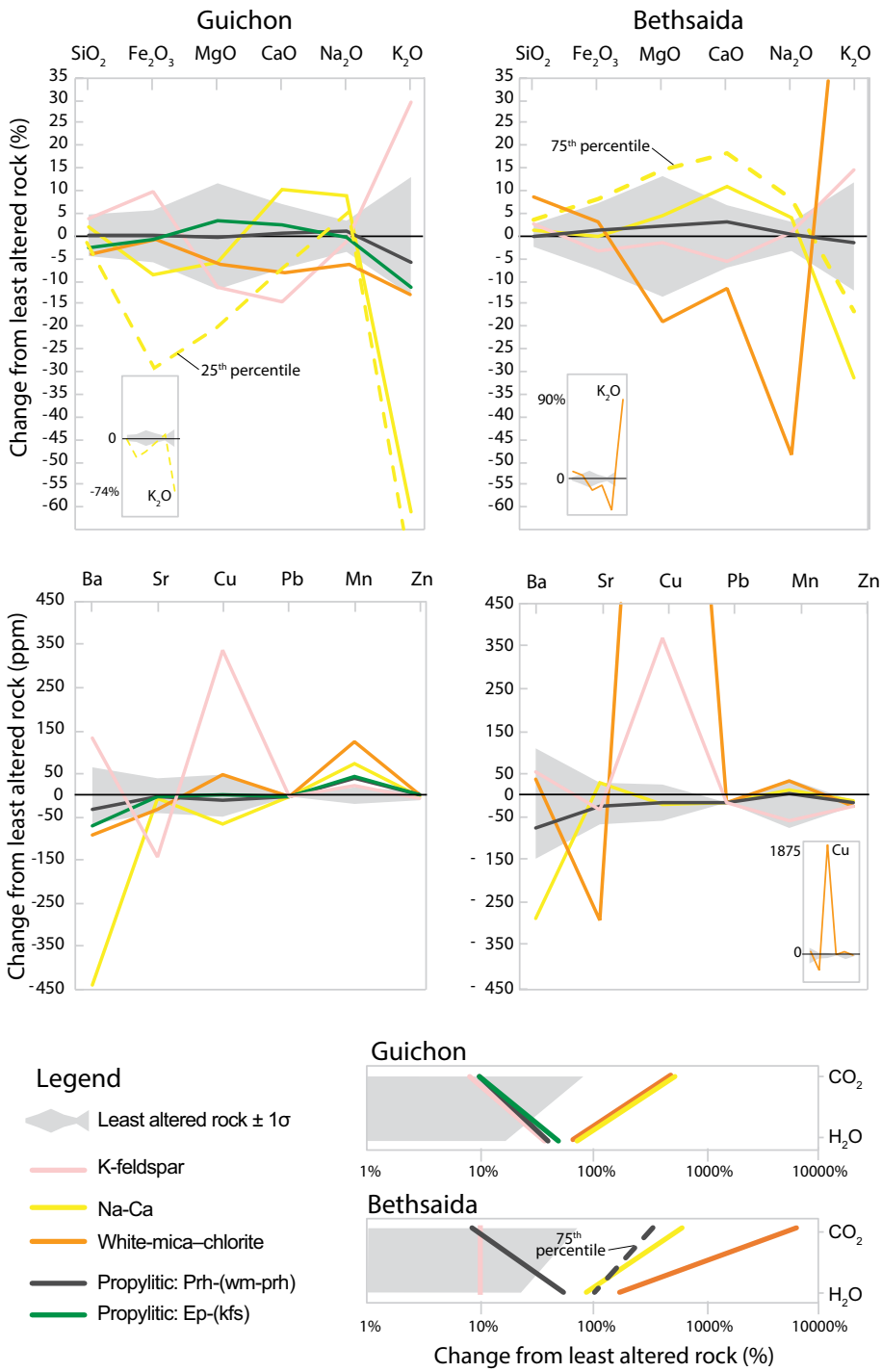

Fig. 12. Material transfer diagrams for the main alteration facies in the Guichon and Bethsaida intrusive phases. Major oxide gains and loss expressed as % change from the least altered rock suite median value. Minor and trace element gains and loss expressed as ppm. Abbreviations: ep = epidote, kfs = K-feldspar, prh = prehnite, wm = white mica.

ognizing alteration peripheral to porphyry Cu centers. The gain and loss of major rock-forming elements during sodic-calcic alteration is more pronounced in the mafic Guichon granodiorite than in the Bethsaida granodiorite (cf. Fig. 12A, C; Table 4). Similarly, the removal of Cu ± Zn, presumably by chlorite alteration of Cu-bearing primary hornblende, is more pronounced in the mafic host rocks (Tables 2, 4; Fig. 12). These phenomena are interpreted to be primarily caused by a larger degree of chemical disequilibrium between the composition of the mafic host rocks and the fluids causing the alteration than between the more felsic rocks and the fluid. Hydrothermal alteration mineralogy is largely dependent on the host-rock bulk composition and the water-rock ratio during exchange (Berger and Velde,

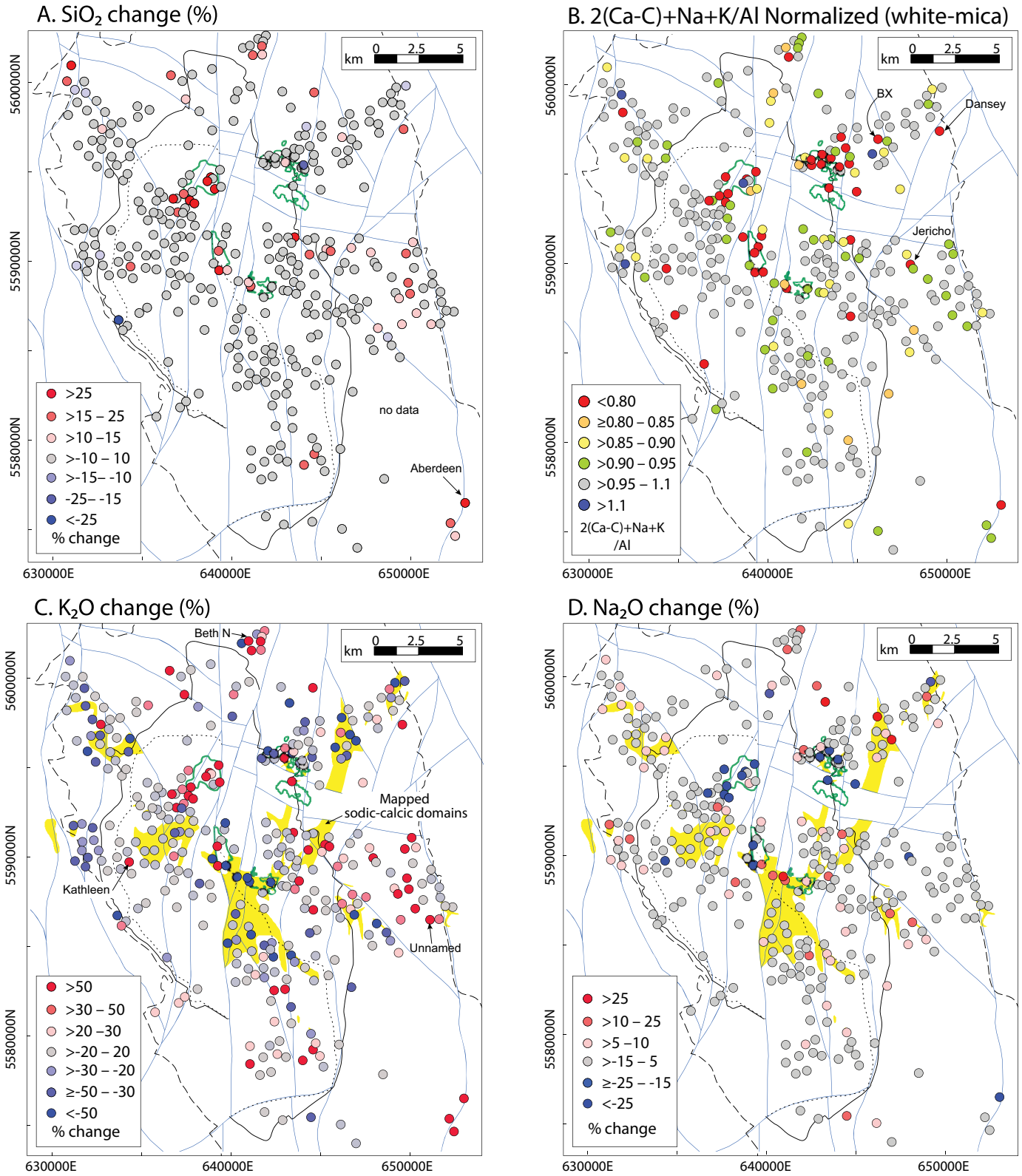

Fig. 13. Alteration intensity and material transfer maps. A. Map of % change in SiO_2. B. (2[Ca-C] + Na + K)/Al values normalized per host rock. There is more abundant white mica in and directly adjacent the Highland Valley Copper porphyry systems. At distances >~1.5 km from mineralization, white-mica alteration is more restricted to structures (e.g., south of Lornex). C. Changes in K_2O and distribution of mapped sodic-calcic alteration. D. Changes in Na_2O and distribution of mapped sodic-calcic alteration. The sample points in all maps were automatically thinned to approximately 400 m spacing for clarity. See Figure 2 for line work explanation.

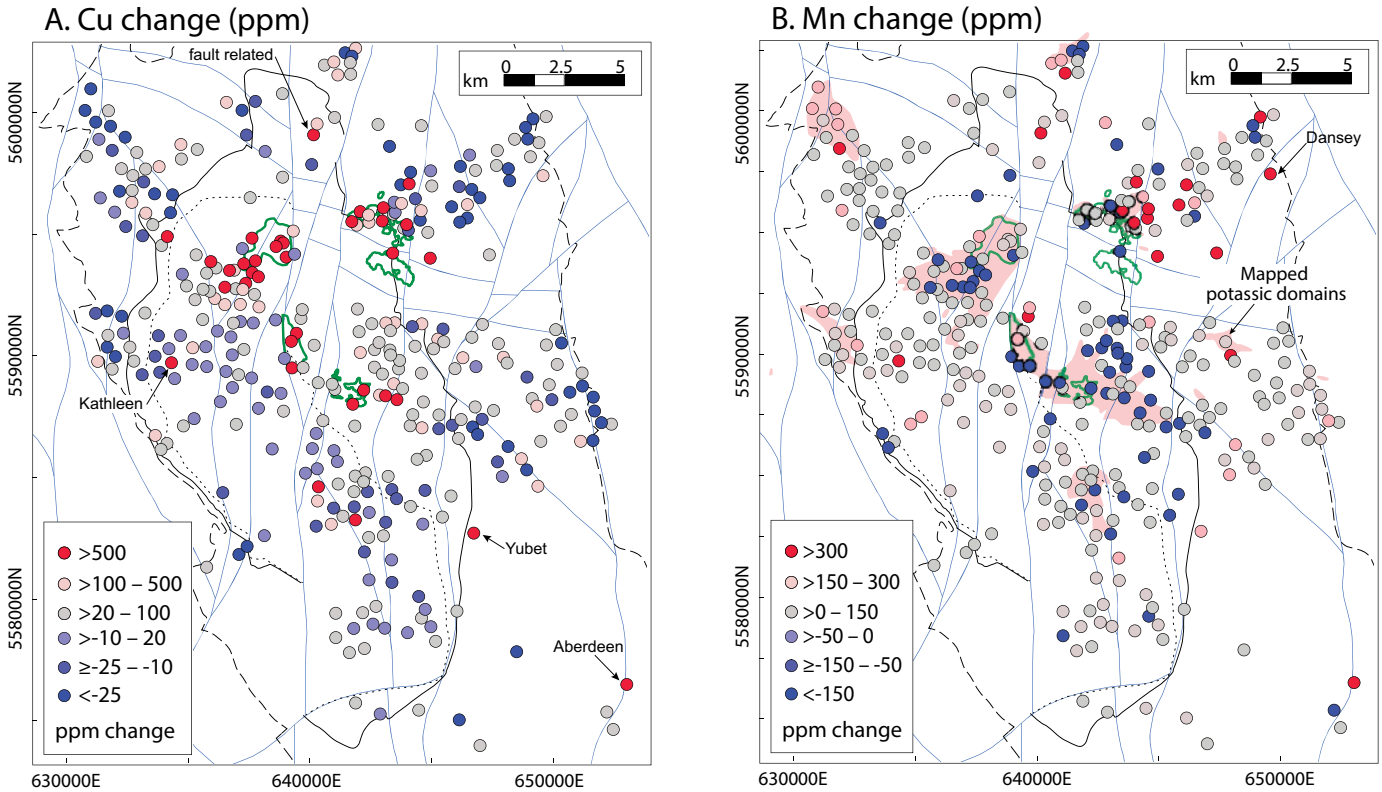

Fig. 14. Minor element material transfer maps. A. Cu (ppm) changes in the Guichon Creek batholith. B. Mn (ppm) changes in the Guichon Creek batholith. The sample points in all maps were automatically thinned to approximately 400 m spacing for clarity. See Figure 2 for line work explanation.

1992; Reed, 1997); while the latter can only be inferred, the host-rock composition can be estimated. Accordingly, in the Guichon Creek batholith, epidote > prehnite veins with propylitic halos are more abundant in the hornblende-dominated mafic host rocks (3.3–5.4 wt % Fe_2O_3; Table 2), rather than in the Fe-poor (2.3 wt % Fe_2O_3; Table 2) and biotite-dominated Bethsaida granodiorite; here, prehnite > epidote veinlets are more common with propylitic alteration (Fig. 2). Prehnite has been rarely reported in propylitically altered rocks around porphyry Cu deposits. Two notable exceptions documented propylitic alteration of basaltic host rocks in the Cadia district (New South Wales, Australia, Wilson et al., 2003) and in andesitic host rocks at Collahuasi (northern Chile, Djouka-Fonkwe et al., 2012). Epidote most commonly forms at temperatures ranging from 200° to 350°C during propylitic alteration (Bowman et al., 1987; Norman et al., 1991). Prehnite and epidote can coexist over a limited temperature range around 250°C; however, the stability field of prehnite expands with decreasing temperature to ~150°C, below which zeolites predominate (Bird et al., 1984; Digel and Gordon, 1995; Bird and Spieler, 2004). In the temperature range of 200° to 350°C, the most important control on the stability of epidote and prehnite in the system CaO-Al_2O_3-Fe_2O_3-SiO_2-H_2O-HCl is the activity of Ca, Fe, and Si, although high activities of CO_2 in the fluid can also inhibit prehnite and epidote formation (Wheeler et al., 2001; Bird and Spieler, 2004). At a fixed temperature, the epidote stability field is larger at higher activities of Fe and lower activities of Ca and Si relative to prehnite (Bird et al., 1984; Digel and Gordon, 1995). On a mineral-stability basis and in rocks with similar Ca content, therefore, epidote formation is favored in a more Fe-rich wall rock. The observations from the Guichon Creek batholith suggests that in Fe-poor and Ca-rich plutonic or volcanic rocks, prehnite veinlets can occur in propylitic alteration zones. Additionally, in the case of epidote-(albite) alteration, the degree of metasomatism may be limited in Fe- and K-poor rocks relative to a host rock that is rich in these elements.

Material transfer and fluid sources

The chemistry of most K-feldspar–altered samples in the Guichon, Chataway, Bethlehem, and Skeena host rocks overlaps with the least altered rock domains, indicating only minor amounts of K were added during alteration (e.g., Fig. 6). A few K-feldspar–altered samples hosted in the Bethsaida unit plot above the least altered rock domain. Around the porphyry Cu centers, generally the material transfer during potassic alteration is minor but can be locally characterized by lower CaO and Mn and higher K_2O, K/Th, and Cu (± Ag) concentrations compared to the least altered rocks. The white-mica–chlorite facies are strongly enriched in K_2O and Cu (and other ore and pathfinder elements; Fig. 12; Table 4), variably enriched in SiO_2, and depleted in Na_2O and CaO in and around the porphyry centers. The material transfer caused by potassic and white-mica–chlo-

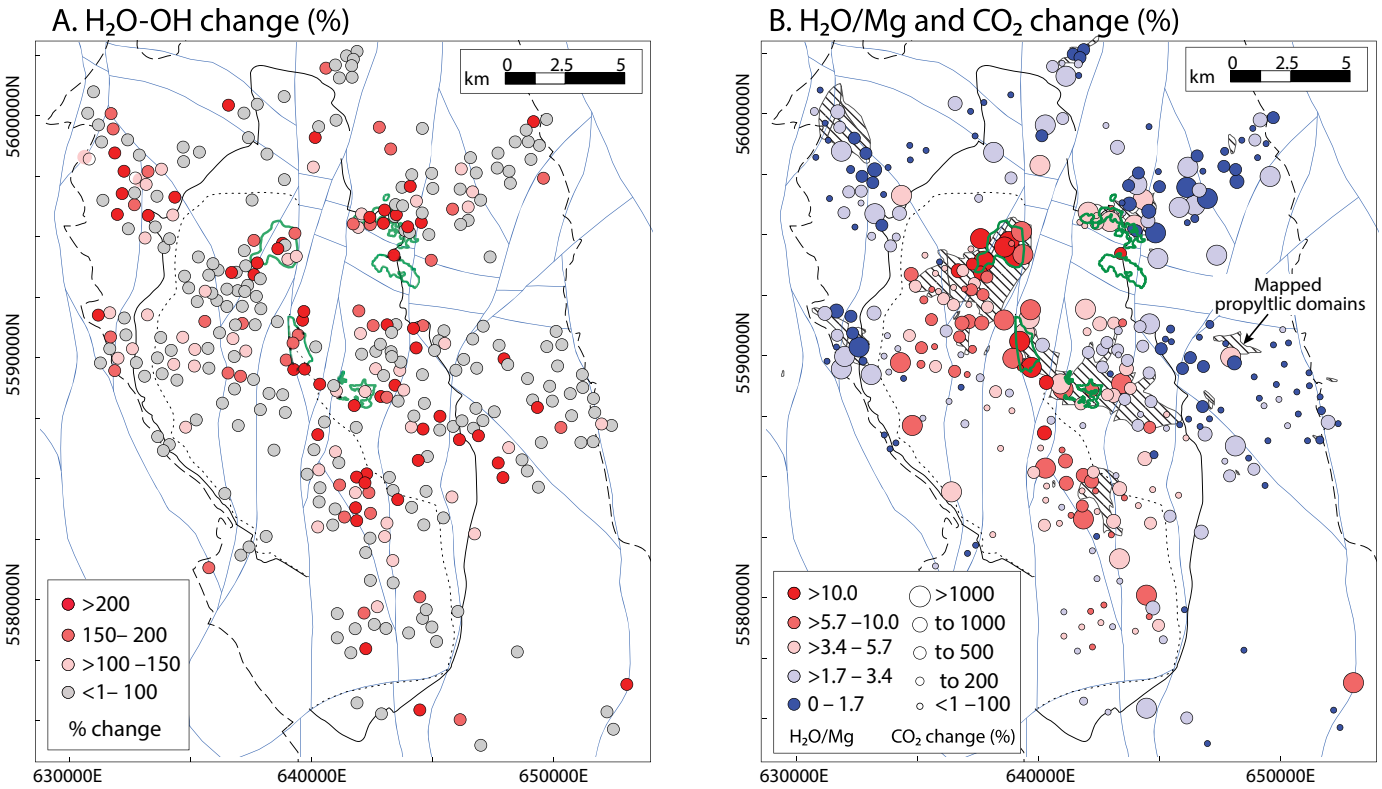

Fig. 15. Material transfer maps. A. Map of % change in H_2O-OH in the Guichon Creek batholith. B. H_2O-OH/Mg and CO_2 addition. The sample points in all maps were automatically thinned to approximately 400 m spacing for clarity. See Figure 2 for line work explanation.

rite alteration is consistent with formation of the alteration assemblages from predominantly magmatic-hydrothermal fluids interacting with the wall rocks (Ulrich and Heinrich, 2001; Sillitoe, 2010).

The sodic-calcic alteration in the Guichon Creek batholith is represented by veins of epidote with albite ± fine-grained white-mica halos principally characterized by depletion in K_2O with varying degrees of Na_2O and CaO addition. Ahmed et al. (2019) also noted that the albite alteration in the Yerington district did not consistently occur with Na addition but was typically associated with >50% CaO addition. A key criterion for the formation of sodic-calcic alteration is the presence of Cl-bearing fluid coupled with a prograding thermal path, which can result in an exchange reaction between primary K-feldspar and secondary albite (Carten, 1986; Dilles and Einaudi, 1992):

$$KAlSi_3O_8 + Na^+_{(aq)} = NaAlSi_3O_8 + K^+_{(aq)}. \quad (2)$$

This reaction is consistent with the mineralogical changes demonstrated by the PER plots and the K loss and localized Na gain during sodic-calcic alteration in the Guichon Creek batholith. Chloritization of biotite can also result in K loss from the host rock. The removal of Fe, Cu, Ag, and Zn during albitization would be facilitated by the heating of a Cl-bearing fluid, because the solubility of these metals increases with increasing temperature (Hemley and Hunt, 1992). In this study we have also shown that Ba and Rb are removed from the rock during albitization, and these elements are inferred to be primarily derived from igneous K-feldspar (Heier, 1962). Based on our data, however, we can only speculate on the fate of the elements mobilized by the fluid during sodic-calcic alteration (i.e., K, Fe, Cu, Ba, and Rb); perhaps they are redeposited in the porphyry center during mixing with magmatic-hydrothermal fluids.

There does not appear to be any significant material transfer of CaO or K_2O during epidote-(K-feldspar) propylitic alteration in the Highland Valley Copper district. The alteration is primarily characterized by the addition of H_2O-OH (10–93%) ± CO_2 (3–465%; Table 4). The K required for the patchy replacement of plagioclase by K-feldspar in vein halos of this facies is interpreted to be locally sourced from biotite during chlorite alteration. Additionally, in order to stabilize secondary K-feldspar over white mica, more alkaline conditions are required for epidote-(K-feldspar) alteration relative to the prehnite-(white-mica–prehnite) subfacies (Hemley and Hunt, 1992). Epidote-(K-feldspar) veins are primarily hosted in Chataway or Guichon granodiorites, and their formation may be related to contact metamorphism and hydrothermal circulation caused by intrusion of the second pulse of magma in the Guichon Creek batholith.

The prehnite-(white-mica–prehnite) propylitic subfacies in the Guichon Creek batholith is associated with the selective replacement of plagioclase by fine-grained white mica and prehnite and chlorite alteration of hornblende and biotite, with only localized calcite formation. These mineral changes are facilitated by the addition of H_2O and CO_2 from the fluid. For discussion purposes, simplified mineral reactions using theoretical mineral compositions are used. Alteration of plagioclase

to form albite, white mica, and prehnite can primarily occur by a hydration reaction:

$$4(Na_{0.5},Ca_{0.5})(Al_{1.5}Si_{2.5})O_8 + K^+_{(aq)} + 4H_2O = NaAlSi_3O_8 + Ca_2Al(AlSi_3O_{10})(OH)_2 + KAl_2(AlSi_3O_{10})(OH)_2 + Na^+_{(aq)} + H_4SiO_{4(aq)}. \quad (3)$$

The K in aqueous solution required for equation (3) is interpreted to have come from the chloritization of primary biotite via a hydrolysis and hydration reaction:

$$2K(Mg,Fe)_3(AlSi_3O_{10})(OH)_2 + 4H^+ + 2H_2O = (Mg,Fe)_5Al(AlSi_3O_{10})(OH)_8 + (Mg,Fe)^{2+}_{(aq)} + 2K^+_{(aq)} + 2SiO_2 + H_4SiO_{4(aq)}. \quad (4)$$

Alternatively, the white mica formed in equation (3) is mostly paragonite, in which case little addition of K is required, and the Na liberated from plagioclase is consumed. The hydration of hornblende and formation of chlorite liberates Ca:

$$Ca_2Mg_4Al(Al_{0.5}Si_3O_{11})_2(OH)_2 + Mg^{2+}_{(aq)} + 2H^+ + 10H_2O = Mg_5Al(AlSi_3O_{10})(OH)_8 + 2Ca^{2+}_{(aq)} + 4H_4SiO_{4(aq)}. \quad (5)$$

The Fe, Mg, Ca, and Si in aqueous solution, derived from fluid-mineral interactions (eq. 3–5), is inferred to be primarily consumed by the formation of prehnite and epidote fracture fills, as there is no significant material transfer of these elements associated with this alteration facies (e.g., Figs. 6, 12). The source of Al for these minerals is unclear, but lab experiments have shown that albitization can locally mobilize Al and Ti (trace levels) from plagioclase via interface-coupled dissolution-reprecipitation at the micron scale (Hövelmann et al., 2010). Additionally, turbidity in feldspars, ubiquitous in the propylitic and sodic-calcic halos in the Guichon Creek batholith, indicates porosity formation (Plümper and Putnis, 2009; Putnis, 2015). Thus, the Al required for minerals precipitated in fractures, as opposed to simply replacing wall rock, is inferred to be locally sourced from feldspars during alteration and concomitant porosity generation in the halo. Nevertheless, it should be noted that at the Guichon Creek batholith, rock compositions do indicate that Al is immobile at the lithogeochemical sample scale (e.g., Figs. 3, 13). Although not accounted for in mass balance calculations, propylitic alteration also caused oxidation of primary magnetite to variable mixtures of hematite and ilmenite and localized reddening within the alteration halo.

Calcite has a retrograde solubility with temperature at fixed pressure, and its precipitation is driven by an increase in fluid pH and CO_2 degassing (e.g., eq. 6), as opposed to fluid cooling (Rimstidt, 1997). Carbonate $\delta^{18}O$ and $\delta^{13}C$ values of about 13 and 4‰, respectively, suggest that the CO_2 fixed in the rocks as calcite is magmatic in origin (Kyser, 1986; Taylor, 1986; Djouka-Fonkwe et al., 2012). Calcite alteration occurs in some rocks associated with white-mica–chlorite facies but mostly manifests as fracture fills. Hydrolysis reactions of feldspar that forms abundant white mica and quartz consume H^+ ions and, thus, promote calcite precipitation:

$$2H_2CO_{3(aq)} + Ca^{2+}_{(aq)} = CaCO_3 + CO_2 + H_2O + 2H^+. \quad (6)$$

This reaction is a plausible mechanism for calcite formation in the white-mica–chlorite facies. However, it is less likely to form calcite in veins in the peripheral parts of the porphyry Cu systems (with lower white-mica content). Phase separation of CO_2 from a late-stage magmatic volatile phase, on the other hand, is more consistent with the paragenesis of calcite in the altered rocks around the Highland Valley Copper porphyry Cu centers. In this case, the Ca required for the formation of calcite in equation (6) could come from the Ca liberated during chloritization of hornblende in propylitic and/or epidote-(albite) domains, or from Ca removed from Cu-mineralized zones associated with white-mica–chlorite facies. Phase separation of CO_2 and calcite formation from a magmatic volatile phase would be enhanced by decompression during a transition from early, high-temperature alteration phases (potassic, sodic-calcic, and early halo-type muscovite), to the lower-temperature and later alteration phases (white-mica–chlorite and propylitic).

Propylitic and sodic-calcic alteration can form from a variety of fluid sources. A common model for the formation of propylitic alteration involves wall-rock reaction with inward-flowing, thermally prograding, meteoric fluids at low water-rock ratio (Meyer and Hemley, 1967; Norman et al., 1991; Reed, 1997). Alternatively, meteoric water with a nonmagmatic brine component (Bowman et al., 1987) or the lateral expulsion of cooling spent magmatic-hydrothermal fluids can generate propylitic alteration peripheral to Cu-bearing potassic or sericite-chlorite alteration domains (Pacey et al., 2020). Sodic-calcic alteration may be caused by the flow of external, hypersaline formation waters (Dilles et al., 1992) or by seawater-sourced fluids (Orovan et al., 2018; Byrne et al., 2020), heated during inflow into the magmatic cupola region along the margins of potassic alteration and porphyry stocks (Dilles et al., 2000). Propylitic alteration around the Highland Valley Copper porphyry centers is interpreted to have formed from a CO_2 degassing, cooling, and spent magmatic volatile phase or from the circulation of an external fluid (or a mixture of both) at moderate water-rock ratios. The overlap of the early sodic-calcic domains with a high density of younger, prehnite-(white-mica–prehnite) veins and alteration (Fig. 2A) and the presence of cogenetic magmatic volatile-derived calcite in the younger alteration suggest that both seawater-derived fluids and magmatic fluids were present peripheral to the Cu centers at Highland Valley Copper at different times (see Byrne et al., 2020). In other porphyry systems, some elements lost from potassic zones (e.g., Ca, Fe, Co) are redistributed outward, producing metasomatic propylitic alteration domains, primarily through the formation of epidote replacement zones (Pacey et al., 2016; Ahmed et al., 2019); thus, a spent and cooling magmatic fluid could conceivably cause localized Ca metasomatism in propylitic domains but perhaps not deplete the rock in K, Fe, and Cu over broad areas.

In summary, this study benefited from a significant number of lithogeochemical samples (850), which allowed us to assess the district-scale mineralogical and geochemical changes. The presented workflow of linking the feldspar staining and SWIR spectral results to the lithogeochemical analyses at Highland Valley Copper shows that the extent of mineralogical change and material transfer is variable for each alteration facies (i.e., Table 4). This variability can be interpreted to be related to a combination of process such as fluid focusing, total fluid flux (water-rock ratio), and the physiochemical gradients between wall rock and fluid. Additionally, our standardized sampling

method, i.e., inclusion of the fresh rock around veins and halo (e.g., Fig. 13A), resulted in lower percent element change relative to least altered host rocks than what would have been achieved if only vein and halo material was included in the sample. As such, we believe the outlined methods will be useful for other studies of, and exploration programs focused on, porphyry Cu systems.

Implications and Conclusions

The workflow presented here—i.e., linking feldspar staining and SWIR spectral results to lithogeochemical analyses—revealed several features of interest: (1) staining highlights weak and cryptic K-feldspar destruction that did not cause sufficient material transfer to be confidently distinguished from protolith compositions; (2) K-feldspar alteration west of the Valley deposit is easily detectable with staining, but generally only caused weak alkali metasomatism; however, this facies is characterized by some SiO_2 addition and higher-than-background Cu and Ag concentrations; (3) SWIR spectral imaging distinguished white mica in samples with an intermediate- to long-wavelength Al-OH feature that is closely related to magmatic fluids and proximal parts of the footprint (see Alva-Jimenez et al., 2020); and (4) staining and spectral imaging identified a subfacies of propylitic alteration, epidote-(K-feldspar), which is probably related to the second magmatic pulse in the Guichon Creek batholith and implies a long history of propylitic (green rock) alteration in the district prior to porphyry Cu mineralization.

We demonstrate that MER and PER diagrams are an effective way to assess subtle mineral changes and material transfer caused by alteration processes but are dependent on correct protolith assignment. Accordingly, careful protolith discrimination using a combination of mapping, textural and mineralogical criteria, and paired immobile elements characteristics (e.g., Al versus Ti, Sc versus Ti, Zr, Th, and Nb) is required. LOI and C and S data can be used to estimate rock H_2O-OH and carbonate mineral concentrations. Furthermore, these data can be easily combined with major oxide determinations to model carbonate (e.g., Fig 9A) and, in some circumstances, sulfide mineral species within the porphyry footprint.

Disparate field and analytical data sets were integrated to identify mappable domains of alteration facies, to quantify material transfer and mineralogical changes, and to detect the total extent of the footprint at Highland Valley Copper. A large area of weak fracture-controlled K-feldspar–dominated potassic alteration developed around the porphyry stocks and barren quartz vein domain (Table 1) and is locally characterized by minor gains in SiO_2, K_2O, and Cu-Ag (Fig. 16, time 1). Localized depletion in K_2O, Fe_2O_3, and Cu and enrichment in Na occur in structurally controlled sodic-calcic alteration domains that formed a large (~34 km^2) nonconcentric footprint outboard of well-mineralized and K-rich zones (Fig. 16, times 2, 3). The sodic-calcic alteration is interpreted to be caused by the heating and inward flow of seawater-derived fluid that mixed with magmatic volatile phases at some of the porphyry centers (Byrne et al., 2020). Well-developed feldspar-destructive white-mica alteration, indicated by (2[Ca-C] + Na + K)/Al values <0.85, addition of SiO_2, K_2O, and Cu-Ag, and depletion in CaO and Na_2O, occurs with quartz-(coarse muscovite) and white-mica–chlorite alteration in the Cu-bearing parts of the porphyry system (Fig. 16, times 2, 3). Outflow of magmatic volatiles from the porphyry centers, coupled with CO_2 degassing, caused incipient calcite precipitation and peripheral white-mica–chlorite alteration with an intermediate to long λ Al-OH absorption position (Fig. 16, time 4). An admixture of externally derived wall-rock equilibrated fluid and CO_2-degassing magmatic volatile phase depleted in ore elements is inferred to have generated propylitic alteration over a large area (~60 km^2) peripheral to the K-rich and Cu-mineralized domains (Fig. 16, time 5). Although interpreted to have formed from seawater-derived fluid, sodic-calcic–altered rocks received a late-magmatic volatile phase flux that is recorded as a series of crosscutting calcite veinlets that is related to porphyry Cu genesis.

Several observations from this study are transferable to other porphyry systems and have exploration implications. Protolith composition influences alteration mineralogy. In calcium-rich and Fe-poor host rocks, prehnite veins with propylitic halos can occur; this may be an underappreciated feature of the footprint in some porphyry systems. If present, sodic-calcic alteration can deplete the protolith in Fe and magnetite concentrations, causing a change in petrophysical properties (e.g., Byrne et al., 2019) that may be detectable using geophysical surveys. At Highland Valley Copper we found that water and magmatic CO_2-rich rocks form the largest coherent lithogeochemical footprint (~60 km^2) that extends beyond domains of enrichment in ore and pathfinder elements and pronounced alkali metasomatism. Recognition of large areas of H_2O and magmatic CO_2-rich rocks in prospective porphyry Cu districts is useful because they indicate the presence of a hydrothermal system, can reduce areas of interest for follow-up target development, help focus mineral chemistry tools (i.e., Baker et al., 2020; Cooke et al., 2020), and potentially provide a vector toward porphyry Cu centers.

Acknowledgments

Funding for this study was provided by the Natural Sciences and Engineering Research Council of Canada (NSERC) and the Canadian Mining Innovation Council (CMIC) through the NSERC Collaborative Research and Development Program. The authors gratefully acknowledge logistical support from Teck Resources Limited and personnel at Highland Valley Copper, as well as financial support from all sponsors of the NSERC-CMIC–funded Mineral Exploration Footprints project. K.B. completed the data analysis and wrote this manuscript. G.L. and K.B. mapped and collected the CMIC rock samples and developed the alteration framework for the district. P.L. collected and interpreted SWIR spectral images. K.B. interpreted, collated, and tabulated feldspar staining results, SWIR mineralogy and textures, and petrographic observations. K.T.K. guided us through the whole-rock isotopic sampling rationale and facilitated data collection at the QFIR. S.J.P. devised the study with K.B. and S.A.G. and critically assessed early versions of this manuscript. We also thank reviewers Shaun Barker and Cliff Stanley for their diligent reviews, which greatly improved the final manuscript. This is NSERC-CMIC Mineral Exploration Footprints project contribution 197.

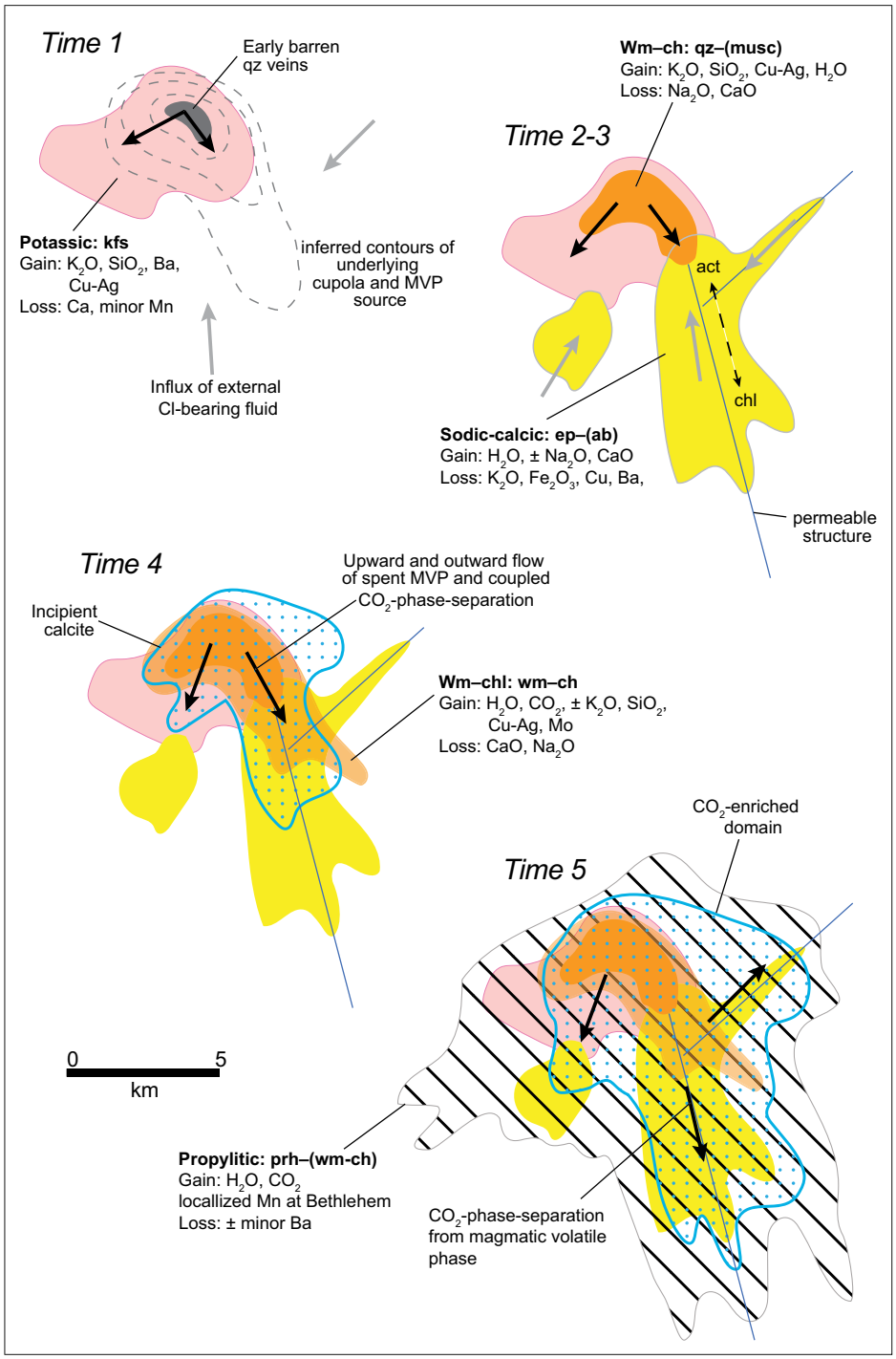

Fig. 16. Time integrated plan maps depicting the evolution of the porphyry Cu footprints at Highland Valley Copper from a lithogeochemical perspective. Abbreviations: ab = albite, act = actinolite, ch = chlorite, ep = epidote, kfs = K-feldspar, musc = muscovite, MVP = magmatic volatile phase, prh = prehnite, qz = quartz, wm = white mica.

REFERENCES

Ager, C.A., McMillan, W.J., and Ulrych, T.J., 1972, Gravity magnetics and geology of the Guichon Creek batholith: British Columbia Department of Mines and Petroleum Resources, Bulletin 62, 31 p.

Ahmed, A.D., Hood, S.B., Gazley, M.F., Cooke, D.R., and Orovan, E.A., 2019, Interpreting element addition and depletion at the Ann Mason porphyry Cu deposit, Nevada, using mapped mass balance patterns: Journal of Geochemical Exploration, v. 196, p. 81–94.

Alva-Jimenez, T., 2011, Variation in hydrothermal muscovite and chlorite composition in the Highland Valley porphyry Cu-Mo district, British Columbia, Canada: M.Sc. thesis, Vancouver, The University of British Columbia, 249 p.

Alva-Jimenez, T., Tosdal, R.M., Dilles, J.H., Dipple, G., Kent, A.J.R., and Halley, S., 2020, Chemical variations in hydrothermal white mica across the Highland Valley porphyry Cu-Mo district, British Columbia, Canada: Economic Geology, v. 115, p. 903–926.

Baker, M.J., Wilkinson, J.J., Wilkinson, C.C., Cooke, D.R., and Ireland, T., 2020, Epidote trace element chemistry as an exploration tool in the Collahuasi district, northern Chile: Economic Geology, v. 115, p. 749–770.

Barrett, T.J., and MacLean, W.H., 1999, Volcanic sequences, lithogeochemistry, and hydrothermal alteration in some biomdal volcanic massive sulfide systems: Reviews in Economic Geology, v. 8, p. 101–131.

Berger, G., and Velde, B., 1992, Chemical parameters controlling the propylitic and argillic alteration process: European Journal of Mineralogy, v. 4, p. 1439–1454.

Bird, D.K., and Spieler, A.R., 2004, Epidote in geothermal systems: Reviews in Mineralogy and Geochemistry, v. 56, p. 235–300.

Bird, D.K., Schiffman, P., Elders, W.A., Williams, A.E., and McDowell, S.D., 1984, Calc-silicate mineralization in active geothermal systems: Economic Geology, v. 79, p. 671–695.

Bowman, J.R., Parry, W.T., Kropp, W.P., and Kruer, S.A., 1987, Chemical and isotopic evolution of hydrothermal solutions at Bingham, Utah: Economic Geology, v. 82, p. 395–428.

Briskey, J.A., 1980, Geology, petrology, and geochemistry of the Jersey, East Jersey, Huestis, and Iona porphyry copper-molybdenum deposits, Highland Valley, British Columbia: Ph.D. thesis, Vancouver, The University of British Columbia, 427 p.

Briskey, J.A., and Bellamy, J.R., 1976, Bethlehem Copper's Jersey, East Jersey, Huestis and Iona deposits: Canadian Institute of Mining and Metallurgy, Special Volume 15, p. 105–119.

Buschette, M.J., and Piercey, S.J., 2016, Hydrothermal alteration and lithogeochemistry of the Boundary volcanogenic massive sulphide deposit, central Newfoundland, Canada: Canadian Journal of Earth Sciences, v. 53, p. 506–527.

Byrne, K., Stock, E., Ryan, J., Johnson, C., Nisenson, J., Alva-Jimenez, T., Lapointe, M., Stewart, H., Grubisa, G., and Sykora, S., 2013, Porphyry Cu-(Mo) deposits in the Highland Valley district, south central British Columbia: Society of Economic Geologists, Guidebook Series, v. 44, p. 99–116.

Byrne, K., Lesage, G., Morris, W.A., Enkin, R.J., Gleeson, S.A., and Lee, R.G., 2019, Variability of outcrop magnetic susceptibility and its relationship to the porphyry Cu centers in the Highland Valley Copper district: Ore Geology Reviews, v. 107, p. 201–217.

Byrne, K., Trumbull, R.B., Lesage, G., Gleeson, S.A., Ryan, J., Kyser, K., and Lee, R.G., 2020, Mineralogical and isotopic characteristics of sodic-calcic alteration in the Highland Valley Copper district, British Columbia, Canada: Implications for fluid sources in porphyry Cu systems: Economic Geology, v. 115, p. 841–870.

Carten, R.B., 1986, Sodium-calcium metasomatism; chemical, temporal, and spatial relationships at the Yerington, Nevada, porphyry copper deposit: Economic Geology, v. 81, p. 1495–1519.

Coney, P.J., Jones, D.L., and Monger, J.W.H., 1980, Cordilleran suspect terranes: Nature, v. 288, p. 329–333.

Cooke, D.R., Hollings, P., Wilkinson, J.J., and Tosdal, R.M., 2014a, Geochemistry of porphyry deposits, *in* Holland, H.D., and Turekian, K.K., eds., Treatise on geochemistry, 2nd ed.: Elsevier, p. 357–381.

Cooke, D.R., Baker, M., Hollings, P., Sweet, G., Zhaoshan, C., Danyushevsky, L., Gilbert, S., Zhou, T., White, N.C., Gemmell, J.B., and Inglis, S., 2014b, New advances in detecting the distal geochemical footprints of porphyry systems: Epidote mineral chemistry as a tool for vectoring and fertility assessments: Society of Economic Geologists, Special Publication 18, p. 127–152.

Cooke, D.R., Wilkinson, J.J., Baker, M., Agnew, P., Phillips, J., Chang, Z., Chen, H., Wilkinson, C.C., Inglis, S., Hollings, P., Zhang, L., Gemmell, J.B., White, N.C., Danyushevsky, L., and Martin, H., 2020, Using mineral chemistry to aid exploration: A case study from the Resolution porphyry Cu-Mo deposit, Arizona: Economic Geology, v. 115, p. 813–840.

D'Angelo, M., 2016, Geochemistry, petrography and mineral chemistry of the Guichon Creek and Nicola batholiths, south-central British Columbia: M.Sc. thesis, Ontario, Canada, Lakehead University, 435 p.

D'Angelo, M., Alfaro, M., Hollings, P., Byrne, K., Piercey, S., and Creaser, R.A., 2017, Petrogenesis and magmatic evolution the Guichon Creek batholith: Highland Valley porphyry Cu ± (Mo) district, south-central British Columbia: Economic Geology, v. 112, p. 1857–1888.

Digel, S.G., and Gordon, T.M., 1995, Phase relations in metabasites and pressure-temperature conditions at the prehnite-pumpellyite to greenschist fades transition, Flin Flon, Manitoba Canada: Geological Society of America, Special Paper 296, p. 67–80.

Dilles, J.H., and Einaudi, M.T., 1992, Wall-rock alteration and hydrothermal flow paths about the Ann-Mason porphyry copper deposit, Nevada; a 6-km vertical reconstruction: Economic Geology, v. 87, p. 1963–2001.

Dilles, J.H., Solomon, G.C., Taylor, H.P., and Einaudi, M.T., 1992, Oxygen and hydrogen isotope characteristics of hydrothermal alteration at the Ann-Mason porphyry copper deposit, Yerington, Nevada: Economic Geology, v. 87, p. 44–63.

Dilles, J.H., Einaudi, M.T., Proffett, J.M., and Barton, M.D., 2000, Overview of the Yerington porphyry copper district: Magmatic to nonmagmatic sources of hydrothermal fluids, their flow paths, alteration affects on rocks, and Cu-Mo-Fe-Au ores: Society of Economic Geologists, Guidebook 32, p. 55–66.

Djouka-Fonkwe, M.L., Kyser, K., Clark, A.H., Urqueta, E., Oates, C.J., and Ihlenfeld, C., 2012, Recognizing propylitic alteration associated with porphyry Cu-Mo deposits in lower greenschist facies metamorphic terrain of the Collahuasi district, northern Chile—implications of petrographic and carbon isotope relationships: Economic Geology, v. 107, p. 1457–1478.

Grant, J.A., 1986, The isocon diagram; a simple solution to Gresens' equation for metasomatic alteration: Economic Geology, v. 81, p. 1976–1982.

——2005, Isocon analysis: A brief review of the method and applications: Physics and Chemistry of the Earth, v. 30, p. 997–1004.

Greenlaw, L., 2014, Surface lithogeochemistry of the Relincho porphyry copper-molybdenum deposit, Atacama region, Chile: M.Sc. thesis, Vancouver, The University of British Columbia, 135 p.

Halley, S.W., Dilles, J.H., and Tosdal, R.M., 2015, Footprints: Hydrothermal alteration and geochemical dispersion around porphyry copper deposits: SEG Newsletter, no. 100, p. 12–17.

Heier, K.S., 1962, Trace elements in feldspars—a review: Norks Geologisk Tidsskrift, v. 42, p. 415–454.

Hemley, J.J., and Hunt, J.P., 1992, Hydrothermal ore-forming processes in the light of studies in rock-buffered systems; II, Some general geologic applications: Economic Geology, v. 87, p. 23–43.

Hollister, V.F., Allen, J.M., Anzalone, S.A., and Seraphim, R.H., 1975, Structural evolution of porphyry mineralization at Highland Valley, British Columbia: Canadian Journal of Earth Sciences, v. 12, p. 807–820.

Hövelmann, J., Putnis, A., Geisler, T., Schmidt, B.C., and Golla-Schindler, U., 2010, The replacement of plagioclase feldspars by albite: Observations from hydrothermal experiments: Contributions to Mineralogy and Petrology, v. 159, p. 43–59.

Jago, C.P., Tosdal, R.M., Cooke, D.R., and Harris, A.C., 2014, Vertical and lateral variation of mineralogy and chemistry in the Early Jurassic Mt. Milligan alkalic porphyry Au-Cu deposit, British Columbia, Canada: Economic Geology, v. 109, p. 1005–1033.

Jambor, J.L., and Delabio, R.N., 1978, Distribution of hydrothermal clay minerals in the Valley copper porphyry deposit, Highland Valley, British Columbia: Geological Survey of Canada, Paper 77-9, 21 p.

Kyser, T.K., 1986, Stable isotope variations in the mantle: Reviews in Mineralogy, v. 16, p. 141–164.

Lee, R.G., Byrne, K., D'Angelo, M., Hart, C.J.R., Hollings, P., Gleeson, S.A., and Alfaro, M., 2020, Using zircon trace element composition to assess porphyry copper potential of the Guichon Creek batholith and Highland Valley Copper deposit, south-central British Columbia: Mineralium Deposita, doi: 10.1007/s00126-020-00961-1.

Lesage, G., Byrne, K., Lypaczewski, P., Lee, R.G., and Hart, C.J.R., 2016, Characterizing the district-scale alteration surrounding a large porphyry Cu system: The footprint of Highland Valley Copper, British Columbia: Geological Association of Canada-Mineralogical Association of Canada (GAC-MAC) Annual Meeting, Whitehorse, Yukon, June 1–3, 2016, Abstracts, v. 39, p. 52.

Lesage, G., Byrne, K., Morris, W.A., Enkin, R.J., Lee, R.G., Mir, R., and Hart, C.J.R., 2019, Interpreting regional 3D fault networks from integrated geological and geophysical data sets: An example from the Guichon Creek batholith, British Columbia: Journal of Structural Geology, v. 119, p. 93–106.

Lesher, M., Hannington, M., Galley, A., Ansdell, K., Astic, T., Banerjee, N., Beauchamp, S., Beaudoin, G., Bertelli, M., Bérubé, C., Beyer, S., Blacklock, N., Byrne, K., Cheng, L.Z., et al., 2017, Integrated multi-parameter exploration footprints of the Canadian Malartic disseminated Au, McArthur River-Millennium unconformity U, and Highland Valley porphyry Cu deposits: Preliminary results from the NSERC-CMIC Mineral Exploration Footprints Research Network: Exploration 17: Sixth Decennial International Conference on Mineral Exploration, Toronto, Ontario, October 22–25, 2017, Proceedings, p. 325–347.

Logan, J.M., and Mihalynuk, M.G., 2014, Tectonic controls on early Mesozoic paired alkaline porphyry deposit belts (Cu-Au ± Ag-Pt-Pd-Mo) within the Canadian Cordillera: Economic Geology, v. 109, p. 827–858.

Lypaczewski, P., and Rivard, B., 2018, Estimating the Mg# and AlVI content

of biotite and chlorite from shortwave infrared reflectance spectroscopy: Predictive equations and recommendations for their use: International Journal of Applied Earth Observation and Geoinformation, v. 68, p. 116–126.

Madeisky, H.E., and Stanley, C.R., 1993, Lithogeochemical exploration of metasomatic zones associated with volcanic-hosted massive sulfide deposits using Pearce element ratio analysis: International Geology Review, v. 35, p. 1121–1148.

McMillan, W.J., 1974, Stratigraphic section from the Jurassic Ashcroft Formation and Triassic Nicola Group contiguous to the Guichon Creek batholith: British Columbia Geological Survey, Geological Fieldwork 1974, p. 27–34.

——1976, Geology and genesis of the Highland Valley ore deposits and the Guichon Creek batholith: Canadian Institute of Mining and Metallurgy, Special Volume 15, p. 85–104.

——1977, Nicola project: British Columbia Geological Survey, Geological Fieldwork 1977, p. 26–36.

——1985a, Geology and ore deposits of the Highland Valley camp: Geological Association of Canada, Field Guide and Reference Manual Series, no. 1, 121 p.

——1985b, J.A. deposit: Geological Association of Canada, Field Guide and Reference Manual Series, no. 1, p. 63–74.

McMillan, W.J., Anderson, R.G., Chen, R., and Chen, W., 2009, Geology and mineral occurrences (MINFILE), the Guichon Creek batholith and Highland Valley porphyry copper district, British Columbia: Geological Survey of Canada, Open File 6079, 2 p.

Meyer, C., and Hemley, J.J., 1967, Wall rock alteration, *in* Barnes, H.L., ed., Geochemistry of hydrothermal ore deposits: New York, Holt, p. 166–235.

Norman, D.K., Parry, W.T., and Bowman, J.R., 1991, Petrology and geochemistry of propylitic alteration at southwest Tintic, Utah: Economic Geology, v. 86, p. 13–28.

Olade, M.A., and Fletcher, W.K., 1975, Primary dispersion of rubidium and strontium around porphyry copper deposits, Highland Valley, British Columbia: Economic Geology, v. 70, p. 15–21.

——1976, Distribution of sulphur and sulphide-iron and copper in bedrock assocaited with porphyry copper deposits, Highland Valley, British Columbia: Journal of Geochemcial Exploration, v. 5, p. 21–30.

Orovan, E.A., Cooke, D.R., Harris, A.C., Ackerman, B., and Lawlis, E., 2018, Geology and isotope geochemistry of the Wainaulo cu-au porphyry deposit, Namosi district, Fiji: Economic Geology, v. 113, p. 133–161.

Pacey, A., Wilkinson, J.J., Boyce, A.J., and Cooke, D.R., 2016, Propylitic alteration and metal mobility in porphyry systems: A case study of the Northparkes Cu-Au deposits, NSW, Australia: Applied Earth Science, v. 125, p. 93–93.

Pacey, A., Wilkinson, J.J., Boyce, A.J., and Millar, I.L., 2020, Magmatic fluids implicated in the formation of propylitic alteration: Oxygen, hydrogen, and strontium isotope constraints from the Northparkes porphyry Cu-Au district, New South Wales, Australia: Economic Geology, v. 115, p. 729–748.

Plümper, O., and Putnis, A., 2009, The complex hydrothermal history of granitic rocks: Multiple feldspar replacement reactions under subsolidus conditions: Journal of Petrology, v. 50, p. 967–987.

Proffett, J.M., 2009, High Cu grades in porphyry Cu deposits and their relationship to emplacement depth of magmatic sources: Geology, v. 37, p. 675–678.

Putnis, A., 2015, Transient porosity resulting from fluid-mineral interaction and its consequences: Reviews in Mineralogy and Geochemistry, v. 80, p. 1–23.

Reed, M.H., 1997, Hydrothermal alteration and its relationship to ore fluid composition, *in* Barnes, H.L., ed., Geochemistry of hydrothermal ore deposits: New York, Wiley, p. 303–365.

Riedell, K.B., and Proffett, J.M., 2014, Batholithic and early halo type Cu-Mo deposits: Geological Society of America, 2014 Annual Meeting and Exposition, Vancouver, British Columbia, October 19, 2014, Proceedings, p. 606.

Rimstidt, J., 1997, Gaunge mineral transport and deposition, *in* Barnes, H.L., ed., Geochemistry of hydrothermal ore deposits: New York, Wiley, p. 487–513.

Roy, B., and Clowes, R.M., 2000, Seismic and potential-field imaging of the Guichon Creek batholith, British Columbia, Canada, to delineate structures hosting porphyry copper deposits: Geophysics, v. 65, p. 1418–1434.

Runyon, S.E., Nickerson, P.A., Seedorff, E., Barton, M.D., Mazdab, F.K., Lecumberri-Sánchez, P., and Steele-Macinnis, M., 2019, Sodic-calcic family of alteration in porphyry systems of Arizona and adjacent New Mexico: Economic Geology, v. 114, p. 745–770.

Russell, K., and Stanley, C.R., 1990, Theory and application of Pearce element ratios to geochemical data analysis: Geological Association of Canada, Short Course Series, v. 8, p. 1–324.

Seedorff, E., Dilles, J.H., Proffett, J.M., Einaudi, M.T., Zurcher, L., Stavast, W.J.A., Johnson, D.A., and Barton, M.D., 2005, Porphyry deposits: Characteristics and origin of hypogene features: Economic Geology 100th Anniversary Volume, p. 251–298.

Seedorff, E., Barton, M.D., Stavast, W.J.A., and Maher, D.J., 2008, Root zones of porphyry systems: Extending the porphyry model to depth: Economic Geology, v. 103, p. 939–956.

Sillitoe, R.H., 2010, Porphyry copper systems: Economic Geology, v. 105, p. 3–41.

——2013, Metallogenic and regulatory inequalities around the northern Pacific Rim: Implications for discovery: Society of Economic Geologists, SEG 2013: Geoscience for Discovery, Whistler, British Columbia, Canada, September 24–27, 2013, Proceedings.

Stanley, C., 2011, Pearce and general element ratio diagrams: Molar scatterplots allowing rigorous investigation of material transfer in geochemical systems: International Applied Geochemistry Symposium, 25th, Rovaniemi, Finland, August 22–26, 2011, Proceedings, p. C10.3.

Stanley, C., and Madeisky, H.E., 1994, Lithogeochemical exploration for hydrothermal ore deposits using Pearce element ratio analysis: Geological Association of Canada, Short Course Notes, v. 11, p. 193–211.

Taylor, B.E., 1986, Magmatic volatiles: Isotopic variation of C, H, and S: Reviews in Mineralogy, v. 16, p. 185–226.

Ulrich, T., and Heinrich, C.A., 2001, Geology and alteration geochemistry of the porphyry Cu-Au deposit at Bajo de la Alumbrera, Argentina: Economic Geology, v. 96, p. 1719–1742.

Urqueta, E., Stanley, C.R., Clark, A.H., Oates, C.J., and Kyser, T.K., 2009, Lithogeochemistry of the Collahuasi porphyry Cu-Mo and epithermal Cu-Ag (-Au) cluster, northern Chile: Pearce element ratio vectors to ore: Geochemistry: Exploration, Environment, Analysis, v. 9, p. 9–17.

Vallée, M.A., Byrne, K., King, J.J., Lee, R.G., Lesage, G., Farquharson, C.G., Chouteau, M., and Enkin, R.J., 2019, Imaging porphyry copper alteration using aeromagnetic data at Highland Valley Copper, British Columbia, Canada: Exploration Geophysics, doi: 10.1080/08123985.2019.1699787.

Warren, I., Simmons, S.F., and Mauk, J.L., 2007, Whole-rock geochemical techniques for evaluating hydrothermal alteration, mass changes, and compositional gradients associated with epithermal Au-Ag mineralization: Economic Geology, v. 102, p. 923–948.

Whalen, J.B., Davis, W.J., and Anderson, R.A., 2017, Temporal and geochemical evolution of the Guichon Creek batholith and Highland Valley porphyry copper district, British Columbia: Implications for generation and tectonic setting of porphyry systems: Geological Survey of Canada, Open File 8334, 45 p., doi: 10.4095/306147.

Wheeler, R.S., Browne, P.R.L., and Rodgers, K.A., 2001, Iron-rich and iron-poor prehnites from the Way Linggo epithermal Au-Ag deposit, southwest Sumatra, and the Heber geothermal field, California: Mineralogical Magazine, v. 65, p. 397–406.

Wilson, A.J., Cooke, D.R., and Harper, B.R., 2003, The Ridgeway gold-copper deposit: A high-grade alkalic porphyry deposit in the Lachlan fold belt, New South Wales, Australia: Economic Geology, v. 98, p. 1637–1666.

Ydon, J.W., 2007, An overview of the economic and geological contexts of Canada's major mineral deposit types: Geological Association of Canada, Mineral Deposits Division, Special Publication 5, p. 3–48.

Kevin Byrne is an exploration geoscientist who has worked in Ireland, Mongolia, Canada, and Chile on projects spanning the mining value chain. He completed his undergraduate degree at Trinity College Dublin (2004), an M.Sc. degree at the University of British Columbia with the Mineral Deposit Research Unit (2009), and a Ph.D. degree at the University of Alberta (2019) that was focused on the footprints of porphyry Cu systems. He has been working for Teck Resources Limited since 2009. He is interested in magmatic and hydrothermal processes, exploration strategy and methods, and the application of integrated geosciences to better predict and model ore and waste-rock characteristics.